Structure-based Design of CDC42 Effector Interaction Inhibitors For the Treatment of Cancer

Sohail Jahid[1]*, Jose A. Ortega[2]*, Linh M. Vuong[1]*, Isabella Maria Acquistapace,[2] Stephanie J. Hachey[5], Jessica L. Flesher[4], Maria Antonietta La Serra[2], Nicoletta Brindani[2], Giuseppina La Sala[2], Jacopo Manigrasso[2], Jose M. Arencibia[2], Sine Mandrup Bertozzi[3], Maria Summa[3], Rosalia Bertorelli[3], Andrea Armirotti[3], Rongsheng Jin[5], Zheng Liu[5], Chi-Fen Chen[1], Robert Edwards[6], Christopher C.W. Hughes[7], Marco De Vivo[2]+, Anand K. Ganesan[1,4]+

[1]Department of Dermatology, University of California, Irvine, Irvine, CA; [2]Laboratory of Molecular Modeling and Drug Design, Istituto Italiano di Tecnologia, Via Morego 30, 16163, Genoa, Italy; [3]Analytical Chemistry and Translational Pharmacology, Istituto Italiano di Tecnologia, Via Morego 30, 16163, Genoa, Italy; [4]Department of Biological Chemistry, University of California, Irvine, Irvine, CA; [5]Department of Physiology and Biophysics, University of California, Irvine, Irvine, CA; [6]Department of Pathology and Lab Medicine, University of California, Irvine, Irvine, CA ; [7]Department of Molecular Biology and Biochemistry, University of California, Irvine, Irvine, CA.

*These authors contributed equally to experimental work

+These collaborating senior authors equally contributed to study design, data analysis, and manuscript preparation

SUMMARY

CDC42 family GTPases (RHOJ, RHOQ, CDC42) are upregulated but rarely mutated in cancer and control both the ability of tumor cells to invade surrounding tissues and the ability of endothelial cells to vascularize tumors. Here we use computer-aided drug design to discover a new chemical entity (ARN22089) that targets CDC42 GTPases and blocks CDC42 effector interactions without affecting the binding between closely related GTPases (RAC1, RAS, RAL) and their downstream effectors. Our lead compound has broad activity against a panel of cancer cell lines, inhibits S6 phosphorylation and MAPK activation, activates pro-inflammatory and apoptotic signaling, and blocks tumor growth and angiogenesis in three-dimensional vascularized microtumor models (VMT) *in vitro*. In addition, ARN22089 has a favorable pharmacokinetic profile and can inhibit the growth of BRAF mutant mouse melanomas and patient-derived xenografts *in vivo*. Taken together, this work identifies a promising new class of therapeutic agents that influence tumor growth by modulating CDC42 signaling in both the tumor cell and its microenvironment.

INTRODUCTION

CDC42 GTPases (RHOJ, RHOQ, CDC42) are linked to multiple human cancers and modulate cell-cycle progression, tumor cell migration/invasion, and tumor angiogenesis.[1] RHOJ, a known regulator of melanoma[2], breast cancer[3], and gastric cancer[4] progression, activates signaling cascades in endothelial cells that are required for tumor angiogenesis[5-7] and induces PAK signaling in tumor cells to promote growth.[2] Similarly, CDC42 is a critical regulator of angiogenic sprouting[8] and tubulogenesis[9] in endothelial cells and promotes tumor cell proliferation and migration.[10] In addition, CDC42 and its downstream PAK kinases are regulators of MAPK inhibitor resistance in BRAF mutant melanoma.[11] Finally, RHOQ, while less studied, is also known to promote tumor invasion[12] and angiogenesis[13].

The GTPase activity of CDC42 family members is tightly regulated by *i)* guanine nucleotide exchange factors (GEFs); *ii)* guanine nucleotide dissociation inhibitors (GDIs); and *iii)* GTPase activating proteins (GAPs).[14] CDC42 activity is also controlled by post-translational modification, including prenylation, which controls membrane localization.[14] CDC42 family members are considered "undruggable" due to their globular structure with limited small molecule binding pockets, and their high affinity for GTP/GDP.[1] Moreover, the tight regulation of CDC42 GTPases by GEFs, GAPs, and GDIs adds an additional level of complexity to targeting these proteins. Nonetheless, recent efforts have focused on developing small molecules that inhibit CDC42 signaling. Existing inhibitors block the ability of GEFs to activate RAC/CDC42[15], prevent RAC/CDC42 from localizing to membranes[16], or block RAC/CDC42 GTP binding[17]. Unfortunately, the efficacy of these strategies is limited by the poor selectivity and/or poor bioavailability of the inhibitors.[1] Furthermore, as CDC42 and RAC1 have overlapping roles in

62 platelet function[18], targeting the signaling of both of these GTPases simultaneously often results
63 in thrombocytopenia *in vivo*[19]. RAC1 also plays an important role in the cardiovascular system,
64 and targeting RAC1 results in cardiotoxicity.[20] New structure-based targeting strategies are
65 needed to develop selective drug-like inhibitors that target the CDC42 family without targeting
66 RAC1 to eliminate potential side effects.
67
68 Recent pioneering work has identified structural pockets in G12C mutant RAS and developed
69 inhibitors that can covalently modify and inhibit G12C RAS function.[21,22] While these approaches
70 can be applied to RAS mutant cancers, they cannot be adapted to target CDC42 as these proteins
71 are rarely mutated. Here we focus on CDC42 and RHOJ, two CDC42 family members that have
72 well-defined roles in cancer. Using a CDC42-PAK6 crystal structure (PDBid: 2ODB), we generate
73 a RHOJ-PAK1 structural homology model and identify a previously unappreciated binding pocket
74 present only in GTP bound CDC42 and RHOJ. We use structure-based virtual screening and
75 molecular dynamics simulations[23] to identify a novel class of compounds that block RHOJ and
76 CDC42 effector interactions, characterize their function *in vitro*, and present proof of principle
77 data that these compounds inhibit tumor growth *in vivo*.
78
79 **RESULTS**
80 **Identification of a Drug Binding Pocket Present in GTP bound RHOJ and CDC42.**
81 To identify putative drug binding pockets in CDC42 family GTPases, we first examined the
82 crystal structure of CDC42 in both its GDP and GTP bound states. When comparing the crystal
83 structures of GDP-bound CDC42 (PDBid: 1DOA)[24] and GTP-bound CDC42 interacting with the
84 CRIB domain of PAK6 (PDBid: 2ODB), we discovered a previously unappreciated allosteric

pocket at the CDC42-PAK6 protein-protein binding interface that is located on the CDC42 surface in proximity to Ser71, Arg68 and Tyr64 (**Fig. 1A,B**). Specific residues of the structural motifs 'switch I '(Val36, Phe37) and 'switch II '(Ala59, Tyr64, Leu67, Leu70, Ser71) on the CDC42 surface, define a pocket ~17 Å away from the GTP binding site, which accommodates the binding of Trp40 on PAK6 (**Fig. 1D**). This pocket is conserved across structures of CDC42 in complex with effectors such as PAK4 (PDBid: 5UPK)[25], PAK1 (PDBid:1EOA)[26], and IQGAP (PDBid:5CJP)[27] - (complete list and structural analyses in **Table S1** and **Fig. S1A,B**). This pocket is also found to be stable during 500ns-long molecular dynamics (MD) simulations of GTP-bound CDC42 ($RMSD_{pocket}$= 2.06 ±0.33 Å, **Fig. S1C**) and is the largest cavity at this protein-protein interface (**Fig. S1E,F**).[28] This distal pocket was unfolded in the CDC42-GDP complex (**Fig. 1B**).

Next, we sought to determine whether this same allosteric pocket could be used to target RHOJ effector interactions. As no crystal structure is available for RHOJ, we built a homology model for RHOJ to use as receptor for a virtual drug screening campaign. The alignment of RHOJ, CDC42, and RHOQ sequences revealed local sequence homology in the domains of RHOJ/RHOQ that interact with its downstream effector PAK, suggesting structural conservation of the pocket (**Fig. 1C-E**). We verified that a similar allosteric binding pocket (involving the interaction of Trp103 of PAK1 with Ser89, Arg86 and Tyr82 of RHOJ)[29] was structurally conserved (**Fig. 1E**) in RHOJ, and stably maintained through additional 500ns-long MD simulations of GTP-bound RHOJ. We observed that the overall structural fold of RHOJ was preserved during these simulations ($RMSD_{RHOJ}$= 1.20 ±0.14 Å; **Fig. S1D**), as it was the allosteric pocket ($RMSD_{pocket}$= 2.07 ±0.27 Å; **Fig. S1D)**. Thus, this allosteric pocket could be targeted to block RHOJ/CDC42 effector

interactions, and is structurally distinct from the CDC42 GEF interaction interface and the K-RAS domains targeted by others (**Fig. S2D-E)**.[30]

Identification of Putative CDC42 Family Effector Interaction Inhibitors

Next we performed a virtual screening campaign of an internal chemical collection of compounds, which contains a diverse and non-redundant set of ~20,000 molecules, to identify RHOJ/CDC42 effector inhibitors. Initially, we selected 54 promising compounds and experimentally tested their IC50s in SKMel28 melanoma cells - a cell line that we previously determined was sensitive to RHOJ depletion (**Fig. 2A**).[29] We then selected compounds with IC50 less than 50 μM (**Table S2**) for further analyses (those with IC50 greater than 50 μM are listed in **Table S3**). We first determined the compounds' ability to inhibit the interaction between RHOJ or CDC42 and its downstream effector PAK using an established CDC42 interaction assay, which measures the interaction between RHOJ/CDC42 and the PAK-p21 binding domain (**Fig. S2B**). We also measured the kinetic solubility of the active compounds to evaluate their potential for further development. Our initial screening campaign identified ARN12405 as a promising hit (IC_{50} of 16.4 μM in SKM28 cell line and high kinetic solubility of 222 μM) that inhibits RHOJ/CDC42-PAK interactions (**Fig. S2B**). Notably, ARN12405 features a functionalized pyrimidine scaffold bearing a 3-piperidine, a 4-chloro aniline, and a 4-pyridine, respectively, in the 2, 4 and 6 position (**Fig. 2B**). Modeling predicts that ARN12405 fits within the effector pocket of RHOJ and CDC42 (**Fig. S2C**). To further assess the predicted binding poses from our docking results, we performed molecular dynamics (MD) simulations of both RHOJ and CDC42 in complex with ARN12405. As shown in **Figure S2F-G, *Left panels***, our hit compound steadily binds the target pocket

129 throughout the simulations ($RMSD_{ARN12405}$ = 2.00 ± 0.40 Å and 3.24 ± 0.85 Å, for RHOJ- and
130 CDC42-ligand complexes, respectively).
131
132 Next we performed hit to lead optimization. We first generated new structural analogues and
133 determined their IC_{50} in five different cancer cell lines (WM3248, Skmel3, A375, SW480,
134 SKM28), as well as kinetic solubility and half-life stability in mouse plasma and in mouse liver
135 microsomes (**Fig. 2A-C,S2A,** synthesis details in Supplemental Information). First, we simplified
136 the starting scaffold to identify the more effective chemical features for RHOJ/CDC42 inhibition,
137 replacing the pyridine heterocycle with a phenyl ring (ARN21698), which slightly increased the
138 activity (IC_{50} 6.3-10.94 μM). Removal or moving the chlorine from para to meta position of the
139 aniline moiety in position 4 (ARN21699, ARN21700), maintaining 4-pyridine, decreased 2 fold
140 the activity compared to the hit in SKM28 cells. Next, we explored additional new aniline
141 substituents while keeping the 3-piperidine heterocycle and the phenyl ring. The replacement of
142 chlorine in para position in ARN21698 by a methoxy (ARN22097) or a dimethyl amino group
143 (ARN22093) resulted in a total or partial loss of activity. In contrast, introducing the same
144 substituents (methoxy and dimethylamino groups) in meta position (ARN22091 and ARN22164)
145 moderately diminished the activity of the compounds. At this point, we moved the piperidine
146 nitrogen from position 3 to 4, keeping either a methoxy or a dimethyl amino substituent in meta
147 position (ARN22090 and ARN22089, respectively – which do not present a chiral center). These
148 compounds are moderately active inhibitors in SKM28 cells (ARN22090 = IC_{50} 38.1 μM,
149 ARN22089 = IC_{50} 24.8 μM). Notably, ARN22089 has a single digit micromolar IC50 activity
150 against the more sensitive cell lines that were tested (WM3248, SKMel3, A375, SW480), an
151 optimal kinetic and thermodynamic solubility (>250 μM and 268 μM, respectively), and a good

half-life in mouse plasma (71 minutes) (**Fig. 2C,S5G**). On the considerations of chemical tractability (synthesis and chirality), inhibitory activity, solubility, and half-life, ARN22089 was elected our lead compound. Modeling predicts that ARN22089 fits within the effector pocket of RHOJ and CDC42 (**Fig. 2E,S2D**). For both RHOJ- and CDC42-ARN22089 complexes, the binding pose is preserved during 500ns-long MD simulations ($RMSD_{ARN22089}$ = 3.55 ± 0.62 Å and 2.80 ± 0.61 Å, for RHOJ- and CDC42-ligand complexes, respectively, **Fig. S2F-G**, ***Right panels***). As a further proof of principle, we examined the ability of the hit compound (ARN12405), of other compounds in the chemical class defined above (ARN21699, ARN22090, ARN22091, ARN22164) and of the lead compound ARN22089 to bind to a purified CDC42 fragment. Initial studies by native mass spectrometry determined that purified CDC42 could be effectively loaded with GDP (90% efficiency of loading) or with the GTP analog, GppNHp (>98% efficiency of loading – **Fig. SH-J**). Then, we observed by microscale thermophoresis that our lead ARN22089 binds better to the purified CDC42 as compared to all other compounds in the class (**Fig. 2D**, MST traces in Supplemental Information **1.8-1.9**), and also when compared to other known CDC42 inhibitors (ZCL278, ML141, R-ketoralac and Casin).[31] Moreover, we found that ARN22089 binds CDC42 preferentially when the protein is the GppNHp loaded state, confirming our modelling results.

ARN22089 is a Selective CDC42 Family Effector Interaction Inhibitor with Anti-Cancer Activity

To gain a better appreciation of the anti-cancer activity of ARN22089, we started by determining the IC_{50} of this compound in a panel of 100 cancer cell lines. Fifty-five of 100 cell lines that were tested had an IC_{50} less than 10 μM (**Fig. 3A**, **Table S4**), demonstrating a broad spectrum of activity

against cancer cells derived from many different tissues. Next, we tested whether our compound was selective for blocking CDC42 family effector interactions in cells. To do this, we tested whether ARN22089 could inhibit the interactions between RHOJ or CDC42 and its downstream effector PAK without affecting the interaction between RAC1 and PAK using an established CDC42 effector assay,[32] which measures the binding between GTPases and their downstream effectors. In parallel, we performed a similar set of experiments to examine the ability of ARN22089 to inhibit the interaction between less closely related members of the RAS family and their downstream effectors.[33] WM3248 cells were treated with the indicated doses of ARN22089, cell lysates were prepared, incubated with EDTA to strip GTP and GDP, followed by incubation with GTP or GDP to load the GTPase, and then incubated with PAK1-p21 binding domain (PAK1-PBD) coupled beads or RAF1-RAS binding domain (RAF1-RBD) coupled beads, which were then precipitated and interacting proteins were identified by immunoblotting. ARN22089 inhibited the interaction between RHOJ or CDC42 and PAK1-PBD at 10 μM and 50 μM concentrations only when cell lysates were incubated with GTP (**Fig. 3B**). No interactions were detected between RHOJ or CDC42 and PAK1-PBD when cell lysates were loaded with GDP (**Fig. 3B**), consistent with previously published work.[2] Notably, ARN22089 did not inhibit the interaction between the most closely related GTPase RAC1 and PAK1-PBD beads or between RAS or RAL and RAF1-RBD beads at either the 10 μM or 50 μM concentrations (**Fig. 3B**), indicating that our lead compound was selective for CDC42 family members and does not inhibit RAC1, RAS, or RAL effector interactions. Our hit compound (ARN12405) similarly blocked RHOJ/CDC42 PAK interaction but not RAC1 PAK interaction (**Fig. S2B**). Taken together, these results indicate that ARN22089 selectively inhibits CDC42 family effector interactions without disrupting signaling

197 from closely related GTPases (RAC1) that are known to be responsible for the cardiotoxicity
198 associated with existing inhibitors of this GTPase family.[20]
199
200 To further validate that ARN22089 inhibits CDC42 effector interactions, we examined whether
201 ARN22089 could inhibit CDC42-PAK interactions in cells. To measure CDC42 effector
202 interactions in cells, we used a BiFluorescence complementation (BiFC) assay,[34] where CDC42 or
203 RHOJ was linked to the N-terminus of Venus fluorescence protein (FP) fragment, while PAK1 is
204 linked to a C terminal Venus FP fragment (**Fig. S3A**). We then measured CDC42/RHOJ PAK
205 interactions by measuring YFP fluorescence in cells. Initial optimization studies revealed that we
206 could visualize GFP indicative of CDC42 PAK interactions in cells that expressed constitutively
207 active (CA) forms of RHOJ/CDC42 and PAK in the presence but not absence of Doxycycline
208 (DOX) which induces the transcription of both proteins (**Fig. S3B**). We next determined the
209 percent intensity of CDC42-PAK interactions using different doses of ARN22089. We observed
210 that ARN22089 could inhibit CDC42-PAK interaction as measured by our BiFC assay with an
211 estimated EC50 of 100 nM (**Fig. 3D, S3C**), consistent with the observation that our hit compound
212 bound to the CDC42 fragment with comparable affinities to compounds with nanomolar affinities
213 (**Fig. 2D**).[1] We observed that ARN22089 could inhibit RHOJ/PAK interactions at an approximate
214 EC50 between 1-5 μM (**Fig. 3E, S3D**), consistent with the IC50s observed in cancer cell lines
215 tested.
216
217 **ARN22089 Inhibits MAPK and S6 Phosphorylation and activates NFkB signaling *in vitro***
218 Published studies indicate that CDC42 GTPases are known to activate a spectrum of signaling
219 cascades. GTP bound CDC42 family GTPases bind to and activate p70S6K.[35] Active p70S6K goes

on to phosphorylate the S6 ribosomal protein at two different locations, 234/235 and 240/244.[36] GTP bound CDC42 family members also activate PAK kinases, whose downstream targets include members of the MAPK and NFkB pathways.[37] To understand the effect of ARN22089 on cells, we first sought to examine how drug treatment influenced the activation of kinase signaling pathways in melanoma cells. WM3248 melanoma cells were treated with 5, 10, or 20 μM ARN22089 for six hours, cell lysates were prepared, and proteins were hybridized with a reverse phase protein array consisting of 486 antibodies to quantitatively examine how the drug influenced protein abundance and protein phosphorylation. This analysis revealed that the compounds were fairly selective, as the abundance of 38 proteins and the phosphorylation of 10 proteins were significantly affected at both the 10 and/or 20 μM doses (**Fig. 4A**, *Left*, **Table. S7**). We observed that ARN22089 could inhibit S6 phosphorylation at both serine 235/236 and 240/244 residues with both 10 and 20 μM doses (**Fig. 4A**, *lower inset*). We also observed that ARN22089 could significantly inhibit phosphorylation at the 235/236 sites in both WM3248 and A375 melanoma cells with 10 and 20 μM doses at 6 hours (**Fig. 4B**) and with a dose of 5 μM at 24 hours (**Fig. 4B**). Another phosphorylation event that was inhibited by ARN22089 was MAPK1 (aka ERK). We observed that ARN22089 inhibited ERK phosphorylation with 10 and 20 μM doses at 6 hours (**Fig. 4B**) and with a 5 μM dose at 24 hours in A375 and WM3248 cells (**Fig. 4B**). Taken together, these studies indicate that ARN22089 is a selective inhibitor of S6 and ERK phosphorylation *in vitro*.

Next, we sought to take a broader view of the pathways engaged by ARN22089. To approach this, we treated cells with either 0, 4, or 6 μM of ARN22089, harvested the cells, and performed RNA sequencing to identify transcripts that were up- or down-regulated upon ARN22089 treatment. We

observed that ARN22089 treatment induced the expression of genes involved in cell death and modulated NFκB signaling (**Fig. 4C,D**, **Table S8**), consistent with the known role of PAK kinases in regulating NFκB signaling [34]. We showed that the RELB protein level is increased with drug treatment compared to untreated cells, corroborating our RNA-seq analysis (**Fig. 4E**). Taken together, these results suggest that ARN22089 inhibits two known CDC42 effector functions- p70S6K activation and PAK activation.

ARN22089 Specifically Inhibits Tumor Angiogenesis in 3D Vascularized Microtumors

CDC42 and RHOJ are both known to have specific roles in tumor angiogenesis. To better understand how ARN22089 impacts tumor angiogenesis, we sought to test the ability of these compounds to inhibit vessel formation around tumors. Here we utilized a vascularized microtumor platform (VMT) - a "tumor-on-a-chip" platform - that incorporates human melanoma cells, which are grown in a 3D extracellular matrix (ECM), and delivers nutrient to the cells via perfused micro-vessels[38-41] (**Fig. S4A-C**). Each chamber of the VMT were loaded with mCherry endothelial cells, GFP labeled tumor cells (A375 and WM3248), fibroblasts, and pericytes. After 4 days, these cells formed a capillary bed that could feed the growing tumor, similar to newly formed vessels *in vivo* (**Fig. S4D**). Nutrients and drug (ARN22089, FRAX597, vehicle) were perfused into the chamber from the high pressure "arterial side" and traversed to the tumor through the vascular network every two days at the indicated doses. The effects of each compound on the number of GFP tumor cells and the length of endothelial vessels was measured. Treatment of VMTs at a concentration of 2 μM ARN22089 inhibited the growth of both A375 cells and the mCherry labeled blood vessels around the tumor (**Fig. 5A**). In contrast, 2 μM FRAX597 did not significantly inhibit the growth of the A375 cells or the blood vessels (**Fig. 5A**). These findings were confirmed in WM3248 cells

266 in which a dose of 2 μM ARN22089 caused significant tumor and vessel regression compared to
267 both control and FRAX treated VMT (**Fig. 5B**). These observations indicate that ARN22089
268 inhibits both tumor growth and angiogenesis.
269
270 Next, we sought to more closely examine whether ARN22089 was a specific inhibitor of tumor
271 angiogenesis. We generated VMTs that contained A375 cells and endothelial cells and VMOs
272 (vascularized micro-organs) that contained vessels but no tumor cells. We observed that
273 ARN22089 could inhibit the growth of both tumor cells and vessels in VMTs at a 600 nM and 2
274 μM doses, significantly more effective than the angiogenesis inhibitor linifanib (**Fig. 5C**). In
275 contrast, ARN22089 did not inhibit the growth of VMOs (**Fig. 5D**). We observed that linifanib, in
276 contrast, did inhibit angiogenesis in VMOs (**Fig. 5D**). These results suggest that ARN22089
277 specifically inhibits tumor and not normal angiogenesis, consistent with the selective role of the
278 CDC42 family member RHOJ in tumor angiogenesis.[6]
279
280 **ARN22089 Has Drug-Like Properties and Inhibits Tumor Growth *in vivo***
281 Once we determined that our RHOJ/CDC42 interaction inhibitor had a broad spectrum of activity
282 *in vitro*, we next determined whether it has drug-like properties. First, we verified that ARN22089
283 has no significant off-target effects as agonist or antagonist for a panel of 47 classical
284 pharmacological targets, even at concentrations up to 25 μM (**Fig. S5A-E**). Notably, ARN22089
285 does not target the hERG channel (**Fig. S5C**), which in other cases has been an impediment in
286 developing safe drugs.[42] We then determined the pharmacokinetics of ARN22089 in experimental
287 animals after intraperitoneal, intravenous, and oral administration (**Fig. 6A**). The compound was
288 well tolerated in experimental animals and had drug-like PK properties (**Fig. 6A, S5F**). In addition,

we incubated the compound with both human and rat liver microsomes and determined that the compound had a half-life of 107 minutes after incubation with rat microsomes and 510 minutes after incubation with human microsomes (**Fig. S5G**).

To test the efficacy of the compound *in vivo*, we first induced BRAF mutant melanoma tumors with topical tamoxifen in *Tyrosinase::CreERT2; Braf$^{CA/+}$; Pten$^{fl/fl}$;RhoJ$^{+/+}$* animals at P21 [2], and treated the mice with ARN22089 for 10 days using a BID, IP dosing regimen. Inhibitor treatment prolonged the survival of tumor carrying mice (mean survival: control 51.5, treated 68.5) (**Fig. 6B**) after only 10 days of treatment. Once we had established that this compound could inhibit the growth of mouse tumors in immunocompetent mice, we next examined the ability of this compound to inhibit the growth of patient-derived xenografts (PDXs) in NOD scid gamma (NSG) mice. Animals were inoculated with PDX tumors, and tumor treatment was initiated after tumors reached a size of 150-200 mm^3. Animals were treated with 10 mg/kg IP BID for two weeks, after which tumors were allowed to continue to grow until they reached endpoint (1500-2000 mm^3). The compound significantly inhibited the growth of 2/5 PDX tumors tested as measured by % tumor growth inhibition and generally inhibited the growth of 4/5 of the tumors tested (**Fig. 6C,S6A**). Interestingly, the PDX models tested included one PDX model that was derived from a patient which had failed both a BRAF inhibitor and immunotherapy, also responded to the treatment (**Fig. S6B**). Histologic evaluation of treated tumors revealed that ARN22089 treatment for 2 weeks increased the amount of tumor necrosis in three of the four tumors that responded to drug (**Fig. S6C,D**). To gauge the effects of long-term ARN22089 treatment on tumor growth, we inoculated mice with one BRAF mutant PDX that was known to have consistent growth properties, and began treating the mice with ARN22089 with 0, 10 mg/kg, or 25 mg/kg IV BIW until control

312 tumors reached endpoint. ARN22089 inhibited tumor growth in a dose responsive manner, without
313 modulating weight of mice (**Fig. 6D,S6E**). We harvested tumors treated at the 0 and 25 mg/kg IV
314 dose and harvested RNA from tumors. RNA-seq analysis of tumors revealed that ARN22089
315 treatment modulated NFκB signaling in 25 mg/kg IV treated tumors, as was observed in *in vitro*
316 treated cells (**Fig. 6E**, **Table S9**). Taken together, these results provide proof of principle that
317 ARN22089 can inhibit tumor growth and vasculogenesis *in vivo* by modulating similar pathways
318 that were observed *in vitro*.
319
320 **DISCUSSION**
321 Targeting CDC42 family GTPases has been difficult secondary to its globular structure and limited
322 small molecule binding pockets,[1] its extensive post-translationally modification in cells,[43] and the
323 fact that these proteins are localized to discrete nanodomains[44]. We took a multipronged approach
324 to identify molecules that would inhibit the protein-protein interaction between CDC42 and its
325 downstream effectors. We identify a structurally conserved, allosteric drug binding pocket that is
326 folded in GTP bound CDC42 and RHOJ, is stable through 500 ns-long molecular dynamic
327 simulations, and is only partially formed and solvent exposed in GDP bound CDC42 (**Fig. 1**). This
328 pocket directly interacts with Trp40 of PAK, indicating that molecules targeting this pocket would
329 inhibit RHOJ/CDC42 and PAK interactions.
330
331 Starting from the discovery of the initial hit compound ARN12405, we built a structure-activity
332 relationship (SAR) study that allowed us to develop the most promising new molecular entity,
333 ARN22089, which we further characterized *in vitro*. First, we verified that: 1) the lead
334 (ARN22089) could bind to CDC42; 2) it bound preferentially to active CDC42; 3) it bound more

335 avidly than other known CDC42 inhibitors (**Fig. 2D**). Second, we examined whether ARN22089
336 has selective activity against CDC42 GTPases. ARN22089 could inhibit the interaction between
337 RHOJ/CDC42 and PAK but did not block the interactions between the closely related RAC1
338 GTPase and PAK or RAS/RAL and Raf at doses as high as 50 μM (**Fig. 3B**). As a further
339 validation, we established a bifluorescence complementation assay, which has been used to
340 measure RHOJ protein-protein interactions,[34] to measure whether our compound could inhibit the
341 protein-protein interaction between RHOJ/CDC42 and PAK1. ARN22089 could inhibit the
342 interaction between RHOJ/CDC42 and PAK1 with an EC50 in the nanomolar range for CDC42
343 and the uni-digit micromolar range for RHOJ (**Fig. 3C,D**).
344
345 Many groups have sought to develop small molecules that inhibit protein-protein interactions,[45]
346 including between Ras family members and their downstream effectors.[46,47] While several of these
347 agents have made it to the clinic, others failed secondary to their suboptimal selectivity and off
348 target-effects.[4] ARN22089 had single digit micromolar EC50s in a panel of cell lines (**Fig. 3A**)
349 consistent with the EC50 values observed with other RAC/CDC42 family inhibitors[48] and non-
350 covalent RAS family protein-protein interaction inhibitors.[46,47] Using a reverse phase protein array,
351 we observed that ARN22089 selectively modulated signaling pathways known to be downstream
352 of CDC42 with little off target effects on other kinase cascades- treatment of cells with 10 or 20
353 μM ARN22089 significantly modulated the expression of only 38 targets and the phosphorylation
354 of only 10 targets (**Table S7**). CDC42 can directly bind and activate p70S6K,[35] inducing the
355 phosphorylation of S6K at 234/235. This specific phosphorylation event was inhibited by
356 ARN22089 (**Fig. 4A**). Moreover, we saw a more potent effect on this phosphorylation event when
357 melanoma cell lines were incubated with this compound for longer times (**Fig. 4B**). PAK kinases

358 can modulate ERK signaling by phosphorylating MEK at Ser298[49] and also by phosphorylating
359 Raf-1.[50] We observed that ARN22089 could inhibit ERK phosphorylation (**Fig. 4A,B**) and block
360 the phosphorylation of MEK at Ser298 (data not shown). Taken together, these data indicate that
361 while ARN22089 has a similar affinity for the protein-protein interaction interface as other drugs,
362 it is highly selective as we observed: 1) no off-target activity as agonist or antagonist against a
363 panel of 47 classical pharmacological targets (**Fig. S5A-E**); 2) a high degree of on-target
364 modulation of CDC42 signaling (**Fig. 4**).
365
366 Several other lines of evidence support the development of ARN22089 as a treatment for cancer.
367 ARN22089 shows excellent solubility and has good chemical and metabolic stability, has a
368 favorable absorption-distribution-metabolism-excretion (ADME) profile *in vitro,* and has
369 favorable pharmacokinetics *in vivo* (intraperitoneral, intravenous, and oral administration).
370 CDC42 family members regulate not only tumor cell proliferation but also tumor
371 angiogenesis.[5,6,14,40] ARN22089 inhibited not only tumor cell growth but also inhibited vessel
372 elongation in three dimensional vascularized tumor models, in contrast to PAK inhibitors, which
373 affect tumor proliferation but not vessel growth (**Fig. 5A-C**). Anti-angiogenic effects were specific
374 for tumor-associated vessels, as ARN22089 had no impact on vessel growth when tumors were
375 not present (**Fig. 5D**). Finally, ARN22089 modulated the expression of genes involved in
376 inflammation and apoptosis (**Fig. 4D,6E**), consistent with a role for the drug in inducing
377 inflammation and apoptosis in tumors.[51]
378
379 Before detailed formulation development, toxicokinetic, and pharmacokinetic characterization of
380 the compound, we wanted to get a sense of the *in vivo* anti-cancer activity of the compound using

a crude formulation. We demonstrated that short term treatment of mice with ARN22089 could prolong survival in a BRAF mutant autochthonous mouse model of melanoma (**Fig. 6B**). In addition, short term treatment could slow the growth of 4/5 BRAF mutant human PDXs to some extent (**Fig. 6C**), including one PDX model that was generated from a BRAF inhibitor resistant tumor (**Fig. S6B**). Drug treatment induced necrosis in treated tumors, a phenomenon that is often observed with angiogenesis inhibitors [52], consistent with the data obtained in the VMT models (**Fig. S6C,D**). Notably, prolonged treatment of tumors with increasing doses of ARN22089 induced more profound tumor growth inhibition, an effect that was dose responsive (**Fig. 6D**). Although further optimization of dosing is still needed, gene expression analysis of tumors revealed that ARN22089 modulates many of the same pathways *in vivo* that were observed *in vitro*. Given the unique spectrum of pathways modulated by ARN22089 and the effects of the drug on the tumor and its microenvironment, this therapy has logical applications both as a primary treatment, as a combination treatment to reduce the dose limiting toxicities of existing agents, or as a treatment for tumors that have developed resistance to other agents. In a broader context, these studies provide a roadmap for the rational structure-based design of drugs targeting other RHO superfamily GTPases for other applications.

MATERIALS AND METHODS

Computations

Homology Modeling.

As a template structure, we employed the CDC42 protein in complex with the CRIB domain of Pak6 (PDB code 2ODB, resolution of 2.4 Å). By means of Prime (Jacobson et al 2004) software implemented in Maestro, we modeled the FASTA sequence of RHOJ on the 2ODB X-ray structure

(i.e., Cdc42 template), and then the resulting structure was refined by using the Protein Preparation Wizard (Sastry et al 2013) workflow implemented in Maestro. According to this procedure, hydrogen atoms were added, and charges and protonation states were assigned titrating the protein at physiologic pH. The steric clashes were relieved by performing a small number of minimization steps, until the RMSD of the non-hydrogen atoms reached 0.30 A.

Virtual screening.

In the CDC42-PAK6 complex, we identified a pocket on the CDC42 surface in proximity of Ser71, Arg68 and Tyr64. Since this surface cavity is conserved in RHOJ, displaying the same residues as in CDC42 (i.e. Ser89, Arg86 and Tyr82), and also the tryptophan is conserved in PAK1, we used this pocket to center the grid. The cubic grid box was centered on Ser89 of RHOJ, having a dimension of 26 × 26 × 26 Å3. We screened a set of nonredundant ~20,000 molecules. These molecules belong to a proprietary chemical collection available in the D3 Department at IIT. The molecules 'database was prepared using LigPrep software implemented in Maestro. Firstly, we added hydrogens and generated ionization states at pH 7.4 ± 0.5. Then, we generated tautomers and all stereochemical isomers. For each structure containing a ring moiety, the low-energy conformation was computed and retained. Lastly, a short minimization step was carried out to relax the 3D structure of each molecule. At this point, we filtered the resulting database to discard molecules that are not endowed with drug-like properties. To do so, we firstly computed the ADME descriptors for each molecule using QikProp software implemented in Maestro. As filter, we discarded all the molecules that do not respect the Lipinsky's rule of five.[53] We used Glide to perform the virtual screening, using Single Precision and retaining one pose for each ligand.

427 **Molecular Dynamics Simulations.**

428 Molecular dynamics (MD) simulations were performed considering both our RhoJ structural
429 model and Cdc42 X-Ray structure (PDBid 2ODB) in their ligand-free state, as well as four
430 different protein-ligand complexes as obtained from our docking calculations. Specifically, two
431 systems were built using our RhoJ structural model bound to either ARN22089 or ARN12405.
432 Other two systems included Cdc42 (PDBid 2ODB) in complex with either ARN22089 or
433 ARN12405. Additionally, the GTP substrate as well as the catalytic Mg^{2+} ion are present at the
434 active site of the proteins, in all the systems. These models were hydrated with a 14Å layer of
435 TIP3P water molecules[54] from the protein center. The coordinates of the water molecules at the
436 catalytic center were taken from PDBid 2ODB. Sodium ions were added to neutralize the charge
437 of the systems. The final models are enclosed in a box of ~89·89·89 Å3, containing ~18,500 water
438 molecules, resulting in ~ 59,000 atoms for each system.
439
440 The AMBER-ff14SB force field[55] was used for the parametrization of the protein. The parameters
441 for the ligands ARN12405 and ARN22089 were determined via Hartree-Fock calculation, with 6-
442 31G* basis set, convergence criterium SCF=Tight after structure optimization (DFT B3LYP
443 functional; 6-31G* basis set). Merz-Singh-Kollman scheme[56] was used for the atomic charge
444 assignment. The GTP and the Mg^{2+} were parametrized according to Meagher KL et al.[57] and Allner
445 et al.[58] respectively. Joung-Chetham parameters[59] were used for monovalent ions.
446
447 All MD simulations were performed with Amber 20[60] and all the systems were object of the
448 following equilibration protocol. To relax the water molecule and the ions, we performed an
449 energy minimization imposing a harmonic potential of 300 kcal/mol Å2 on the backbone, the GTP

and the docked compound, when present. Then, two consecutive MD simulations in NVT and NPT ensembles (1 ns and 10 ns, respectively) were carried out, imposing the previous positional restraints. To relax the solute, two additional energy minimizations steps were performed imposing positional restraints of 20 kcal/mol Å2 and without any restraints, respectively. Such minimized systems were heated up to 303 K with four consecutive MD simulations in NVT (~0.1 ns, 100 K) and NPT ensembles (~0.1 ns, 100 K; ~0.1 ns, 200 K; ~0.2 ns, 303 K), imposing the previous positional restraints of 20 kcal/mol Å2. We used the Andersen-like temperature-coupling scheme[61] while pressure control was achieved with Monte Carlo barostat at reference pressure of 1 atm. Long-range electrostatics were treated with particle mesh Ewald method. We performed an additional MD simulation (~1.5 ns) in the NPT ensemble at 303 K without any restraint to relax the system at such temperature. Finally, multiple replicas of 500 ns were performed in the NPT ensemble for each system with an integration time step of 2 fs.

His-Cdc42 production and purification

His-Cdc42 wild-type (aminoacids Ile4-Pro182) was expressed in *E. coli* BL21 (DE3) cells using the pET28a expression vector. Overexpression was induced by 0.1 mM IPTG at OD_{600} 0.8 in Luria Bertani broth and incubated over night at 18 °C. Cells were harvested by centrifugation at 6000 xg for 30 min and the pellet was stored at – 80 °C. Cells were defrosted by incubation at room temperature in 50 mM Tris-Cl buffer pH 7.5, 400 mM NaCl, 5 mM $MgCl_2$, 50 µM GDP, 40 mM imidazole, 10 µg/ml DNAse (Sigma) and 30 µg/ml Lysozyme (Sigma). Cells were lysed by sonication and centrifuged at 43000 xg at 4 °C for 1 h. The supernatant was incubated for 3h at 4 °C, rotating, with Ni-NTA resin prior in batch purification. His-Cdc42 was eluted with 300 mM imidazole.

Preparation of GppNHP/GDP-bound GTPase

For the loading of GDP, the purified protein was dialyzed over night at 4 °C in 50 mM Tris pH 8.5, 200 mM ammonium sulfate, 50 µM GDP (Jena Bioscience). For the loading of GppNHp, His-Cdc42 was instead dialyzed with 20 µM GppNHp (Jena Bioscience) in the presence of 5 U of Quick-CIP alkaline phosphatase (New England Biolabs). After dialysis, 2 mM $MgCl_2$ was added to the solution to stabilize nucleotide binding. The two samples were buffer exchanged in 20 mM Hepes pH 7.5, 40 mM NaCl, 5 mM $MgCl_2$, 1 mM DTT and loaded on a RESOURCE Q (Cytiva) column for anion exchange chromatography. The efficiency of nucleotide loading was evaluated by native state mass spectrometry.[62] The purified proteins were buffer exchanged in 10 mM ammonium acetate pH 6.8 and diluted to 3 µM in 10 mM ammonium bicarbonate pH 6.5 added with final 3% acetonitrile. The samples were then infused at 40 µL/min in an electrospray ion source, coupled to a Synapt G2 QToF mass spectrometer operating in positive ion mode. Spectra were acquired over the 500-4000 m/z range.

Target binding by microscale thermophoresis

MicroScale Thermophoresis (MST) experiments were performed according to the NanoTemper technologies protocols in a Monolith NT.115 Pico (Pico Red / Nano Blue - NanoTemper Technologies). His-Cdc42 affinity for the RED-tris-NTA label was not optimal therefore Alexa Fluor 647– NHS dye was used. His-Cdc42 was labeled following the instructions of the MO-L001 Monolith NT Protein Labeling Kit RED – NHS (NanoTemper Technologies). Labelled protein concentration in the binding reactions was 10 nM while compounds concentration was either 50 or 100 µM. DMSO concentration was maintained constant across samples at either 0.5 % or 1 %. Solutions were prepared in 100 mM Trizma® base (Sigma) pH 7.5, 40 mM NaCl, 0.05% v/v Tween 20 and incubated 5 min before loading on Premium Capillaries and analysis. Binding was

496 detected at 24 °C, MST power high and 20% LED power. The MST traces were recorded as
497 follows: 3 s MST power off, 20 s MST power on and 1 s MST power off. The difference in
498 normalised fluorescence (ΔF_{norm} [%]= F_{hot}/F_{cold}) between protein:compound sample and a protein
499 only sample at 1.5-2-5 sec is calculated and plotted through MO.Affinity analysis v2.3
500 (NanoTemper Technologies) and GraphPad Prism 8.0.0 (GraphPad Software, San Diego,
501 California USA). Signal to noise ratio was used to evaluate the quality of the binding data
502 according to NanoPedia instructions (NanoTemper Technologies). Only a signal-to-noise ratio of
503 more than 5 was considered acceptable while a signal to noise of more than 12 was considered
504 excellent.

505 **CDC42 interaction assay**

506 A CDC42 activation assay was performed according the manufacturer's protocol (Cell Biolabs,
507 San Diego, CA) as described previously [2]. Briefly, cells expressing high RHOJ (WM3248 or
508 WM983B) were treated with ARN22089 at the indicated doses. 24 hours later the lysates from
509 treated and untreated cells were unloaded of guanosine nucleotides and either loaded with GDP or
510 GTPγS. Agarose beads conjugated with the PAK1 PBD or RAF RBD were used in pull down
511 assays for RHOJ, CDC42, RAC1 or RAS and RAL, respectively. Precipitated lysates were then
512 immunoblotted with indicated antibodies.

513

514 **Immunoblotting**

515 Melanoma cells treated with ARN22089 for 6 or 24 h and lysed in RIPA buffer (EMD Millipore
516 or an optimized cocktail (250 mM NaCL, 50 mM TrisCL pH 7.5, 0125% Nadeoxycholate, 0.375%
517 Triton-X100, 0.15% NP-40, 4 mM EDTA) containing protease and phosphatase inhibitors cocktail

(Thermo Scientific) and 1 mM PMSF and DTT. Lysates were then subjected to SDS-PAGE, transferred to PVDF membranes, followed by incubation with the indicated primary antibody and appropriate HRP-secondary antibody. ImageJ was used to perform densitometry.

A375 cells were maintained in DMEM (plus high glucose, L-glutamine, sodium pyruvate) supplemented with 10% FBS, 1% MEM NEAA and 1% antibiotic-antimycotic. WM3248 cells were maintained in 80% MCDB153 pH 7.30, 20% Leibovitz's L-15, 2% FBS, 5 ug/mL insulin (bovine), 1.68 mM $CaCl_2$, and 1% antibiotic-antimycotic. All cells kept in 5% CO_2 incubator at 37^{o}C.

Reverse Phase Protein Arrays (RPPA)

Melanoma cells (WM3248) were seeded at 3.6 x 10^6 cells per 150 mm plate and, 24 h later, treated with ARN22089 at 0, 5, 10, or 20 μM. Six hours later, cells were scraped and centrifuged at 1.3 KRPM for 15 min cold (between 4-16^{o}C range). Pellets were snapped freeze in liquid nitrogen and shipped to MD Anderson Cancer Center core RPPA facility for RPPA analysis (**Table S5**). Three biological replicates for each sample were generated.

Multiple t test in Prism8 software was used to determine proteins with significant difference between 0 and 5, 10 or 20 μM. Normalized linear values were used to perform the t test with the following parameters: (1) Individual P values were computed with fewer assumptions by analyzing each row individually and did not assume consistent standard deviation; (2) Multiple comparisons were not corrected for; (3) alpha 0.05 was selected.

Heatmaps of RPPA represent normalized values (normalized linear values of 5, 10 or 20 μM divided by normalized linear values of 0 μM) (**Table S5-7**). Nomenclatures on the RPPA heatmaps: name_of_antibody.species_of_antibody.status_of_antibody. V - antibody validated; C

- validation of antibody in progress; Q - antibody nonspecific; E - under evaluation; antibodies raised in M - mouse, G - goat, R - rabbit, or T - rat.

RNA-seq analysis

WM3248 melanoma cells were seeded at 8.4 x 10^4 cells. The next day, cells were treated with ARN22089 at 0, 4, or 6 μM and harvested 24 h later by adding RLT lysis buffer (Qiagen). Similarly, a small chunk of PDX tumor was collected and lysed in RLT lysis buffer. RNA was extracted using a RNeasy kit (Qiagen) and sent to the Genomic Core Facility at UCI for library construction and sequencing.

For the cell lines, paired-end sequencing reads were aligned to the human reference genome (GRCh37/hg19) with Tophat v2.1 (used in conjunction with Bowtie2 v2.2.7 and Samtools v1.9) and processed with Tuxedo Suite (Cufflinks v2.2.1).[63,64] Heatmaps and other visualizations were generated using CummeRbund in R v4.0.3.

For PDX tumors, paired-end sequencing reads were aligned to both human and mouse reference genome (NCBI/GRCh38 and UCSC/mm10, respectively) using HISAT2 v2.1.0[65]; and Samtools v0.1.19 to convert to bam files and sort. Then XenofilteR[66] was used to remove mouse reads, and reads were counted using featureCounts (subread v1.5.0-p3). Differential expression analysis was done using DESeq2[67] in R.

Additional analyses of gene expressions were performed using STRING ('Search Tool for Retrieval of Interacting Genes/Proteins') and DAVID ('Database for Annotation, Visualization hand Integrated Discovery') to determine protein-protein network and functional annotation.[68,69]

Bi-fluorescence Complementation Assay

564 Inducible HEK293 Flp-In T-REx cell line was a gift from Dr. Jean-Francois Cote in the Montreal
565 Clinical Research Institute (IRCM), Montreal, Quebec, Canada.[70] Cells were maintained in
566 DMEM supplemented with 10% fetal bovine serum (TET tested, heat inactivated, R&D
567 SYSTEMS INC), 1% antibiotic-antimycotic, 10 µg/mL blasticidin and 100 µg/mL zeocin at 37°C
568 in 5% CO_2. Stable BiFC lines were generated by co-transfecting pOG44 and pKK-BiFC-Venus-
569 CDC42/RHOJ-PAK1 plasmids (9:1 ratio) and selecting with 100 µg/mL hygromycin and 10
570 µg/mL blasticidin 24-48 h after transfection. The CDC42 and RHOJ genes in the pKK-BiFC-
571 Venus-CDC42/RHOJ-PAK1 plasmid, the following residues were modified to generate
572 constitutively active form: CDC42, Q61L; RHOJ, Q79L.[71,72]
573 For CDC42 constitutively active (CA) assays, cells were seeded at 0.5 x 10^5 cells per well of a 4-
574 chamber slide. The next day, cells were treated with indicated doses and induced with 2 µg/mL
575 doxycycline (DOX), simultaneously. Twenty-four hours later, cells were washed in PBS and fixed
576 with 4% para-formaldehyde and 0.10% Triton-X100 in PBS for 15-20 min. Cells were then
577 washed with PBS and incubated with blocking buffer (10% goat serum in PBS) for 30 min at RT
578 and incubated with primary antibody (anti-GFP Invitrogen chicken Y fraction) at 1:1000 in
579 blocking buffer 4 h RT, slow nutating. Cells were washed once with PBS buffer for 5 min.
580 Secondary antibody (Alexa 488 nm) at 1:1000 in blocking buffer and cells were incubated for 1 h
581 at RT, followed by DAPI 1:1000 in PBS for 20 min at RT. Cells were washed 3 times with PBS
582 buffer, each time 5 min at RT. Slides were mounted with mounting medium (Vectorshield).
583 For RHOJ CA assays, cells were seeded at 1.5 x 10^5 cells per well of a 4-chamber slide. Next day,
584 cells were treated with indicated doses and induced with 2 µg/mL doxycycline (DOX),
585 simultaneously. Eight hours later, cells were washed in PBS and fixed with 4% para-formaldehyde
586 and 0.10% Triton-X100 in PBS for 15-20 min. Subsequent steps both clones were processed the

same. Cells were then washed with PBS and incubated with blocking buffer (10% goat serum in 1 x PBS) for 30 min at RT and incubated with primary antibody (anti-GFP Invitrogen chicken Y fraction) at 1:2000 in blocking buffer overnight at 4°C, slow nutating. Cells were washed once with PBS buffer for 5 min. Secondary antibody (Alexa 488 nm) at 1:1000 in blocking buffer and cells were incubated for 1 h at RT, followed by DAPI 1:1000 in PBS for 20 min at RT. Cells were washed 3 times with PBS buffer, each time 5 min at RT. Slides were mounted with mounting medium (Vectorshield).

Slides were viewed using the Keyence BZ-X810 Wide-Field Microscope in the Stem Cell Research Center at the University of California, Irvine (UCI). Images were captured at high resolution with the same exposure time. Fluorescent images were quantified using Imaris software (BitPlane). Measurement setting includes surface masking [parameters: segment only a region of interest (excluding bright and blurry spots), classify surfaces, object-object statistics] to measure absolute intensity (threshold intensity adjusted for each image), and filter was set to "Number of Voxels Img=1" > 10. Intensity mean of all areas average from 5-6 images per condition at 20 x magnification. Percent average intensity mean was calculated as follow: ((Dose_1-NoDOX)/(DOX-NoDOX)) x 100). The standard error of mean was calculated taking the percent mean of intensity mean and divided by the square root of the number of surface areas measured.

Vascularized Microtumor Assay

Methods for microfluidic device fabrication and establishing VMTs have been described previously (Sobrino 2016). Briefly, human endothelial colony-forming cell-derived endothelial cells (ECFC-EC) are isolated from cord blood via selection for the CD31+ cell population and cultured in EGM2 medium (Lonza). Normal human lung fibroblasts (LF) are purchased from

Lonza. Cancer cells and LF are cultured in DMEM (Corning) containing 10% FBS (Gemini Bio). The ECFC-EC and cancer cells were transduced with lentivirus expressing mCherry (LeGO-C2, plasmid # 27339) or green fluorescent protein (GFP) (LeGO-V2, plasmid # 27340) (Addgene, Cambridge, Massachusetts). To load the microfluidic device, ECFC-EC and LF (both 8 x 10^6 cells/mL) and cancer cells (2.5 × 10^6 cells/mL) were resuspended in fibrinogen solution (10 mg/mL basal medium). The cell slurry was then mixed with 1 μL thrombin (3 U/mL) to catalyze gel solidification and quickly loaded into the tissue chambers of each VMT unit. Fibrin ECM was allowed to solidify at 37°C for 15 minutes prior to introducing ECM and EGM2 medium through the microfluidic channels. All cells and VMTs are cultured in a 37 °C, 20% O2, 5% O2 environment.

Vascularized Microtumor Treatment

After culturing for 5 days to allow full development of each VMT, culture medium is replaced by medium containing the drugs (ARN22089, FRAX or vehicle) at the desired concentration and delivered through the microfluidic channels using the hydrostatic pressure gradient. Fluorescence images were acquired with an Olympus IX70 inverted microscope using SPOT software (SPOT Imaging, Sterling Heights, Michigan). AngioTool software (National Cancer Institute) was used to quantify vessel length in the VMT and ImageJ software (National Institutes of Health) was utilized to measure the total fluorescence intensity (i.e. mean grey value) for each tumor image to quantify tumor growth. Each chamber was normalized to time 0 baseline.

Cancer cell line viability assay

Cancer cell line viability assay was performed by Proqinase with ARN22089 that we provided. Cells were cultured in their appropriate media and seeded in white multi-well plates. For the assays, cells were incubated with compound at 37°C overnight before compound was added. Cells were incubated in compound for 72 hours, and a CellTiterGlo assay was performed to quantify viable cells. The IC_{50} was calculated in a panel of 100 cell lines.

PK Determination

ARN22089 was administered at 10 mg/kg PO and IP, while it was injected at 3 mg/kg IV to male mice. The vehicle for all administration routes was PEG400/Tween 80/Saline solution at 10/10/80% in volume, respectively. Three animals per dose/time point were treated, and blood samples were collected at selected time points up to 480 min. Plasma was separated from blood by centrifugation for 15 min at 1500 rpm a 4°C, collected in eppendorf tubes and frozen (-80°C). Control animals treated with vehicle only were also included in the experimental protocol. Plasma samples were centrifuged at 21.100 g for 15 min at 4°C. A 50 µl aliquot was transferred into a 96-Deep Well plate and 150 µl of extraction solution was added. The extraction solution was consisting of cold CH3CN spiked with 200 nM of internal standard. The plate was centrifuged at 21.100 g for 15 min at 4°C. Eight microliters of supernatant were then transferred into a 96-Deep Well plate and 80µl of H2O was added. A reference standard of the compound was spiked in naïve mouse plasma to prepare a calibration curve over a 1 nM – 10 µM range. Three quality control samples were prepared by spiking the compound in blank mouse plasma to the final concentrations of 20, 200 and 2000 nM. Calibrators and quality controls were extracted with the same extraction solution used for the plasma samples. The samples were analyzed on a Waters ACQUITY UPLC/MS TQD system (Waters Inc. Milford, USA) consisting of a TQD (Triple Quadrupole

Detector) Mass Spectrometer equipped with an Electrospray Ionization interface and a Photodiode Array eλ Detector. The analyses were run on an ACQUITY UPLC BEH C18 (50 x 2.1 mmID, particle size 1.7 µm) with a VanGuard BEH C18 pre-column (5 x 2.1 mmID, particle size 1.7 µm) at 40°C. 0.1% HCOOH in H2O (A) and 0.1% HCOOH in CH3CN (B) were used as mobile phase with a linear gradient from 50 to 100% B in 2 min with the flow rate set to 0.5 mL/min. Electrospray ionization was applied in positive mode. Plasma levels of the parent compound was quantified by monitoring the MRM peak areas.

Aqueous kinetic solubility assay

The aqueous kinetic solubility was determined from a 10mM DMSO stock solution of test compound in Phosphate Buffered Saline (PBS) at pH 7.4. The study was performed by incubation of an aliquot of 10mM DMSO stock solution in PBS (pH 7.4) at a target concentration of 250 µM resulting in a final concentration of 2.5% DMSO. The incubation was carried out under shaking at 25°C for 24 h followed by centrifugation at 14.800 rpm for 30 min. The supernatant was analyzed by UPLC/MS for the quantification of dissolved compound (in µM) by UV at a specific wavelength (215 nm). The UPLC/MS analyses were performed on a Waters ACQUITY UPLC/MS system consisting of a Single Quadrupole Detector (SQD) Mass Spectrometer (MS) equipped with an Electrospray Ionization (ESI) interface and a Photodiode Array Detector (PDA). The PDA range was 210-400 nm. ESI in positive mode was used in the mass scan range 100-650 Da. The analyses were run on an ACQUITY UPLC BEH C18 column (50 x2.1 mmID, particle size 1.7 µm) with a VanGuard BEH C18 pre-column (5 x 2.1 mmID, particle size 1.7 µm), using 10 mM NH_4OAc in H_2O at pH 5 adjusted with AcOH (A) and 10mM NH_4OAc in CH_3CN-H_2O (95:5) at pH 5 (B) as mobile phase.

678 The thermodynamic solubility was determined by addition of Phosphate Buffered Saline (PBS) at
679 pH 7.4 to an excess of solid test compound. The study was performed by incubation of an aliquot
680 of 2.5mg of test compound in 500µL of PBS at pH 7.4 (final target concentration: 5mg/mL). The
681 suspension was shaken at 300rpm for 24h at 25°C. The pH of the suspension was measured at the
682 beginning and at the end of the incubation. At the end of the incubation, the saturated solution was
683 filtered and analyzed by LC-MS for the quantification of dissolved compound by UV at 254nm
684 using a calibration curve. The analyses were performed on a Waters ACQUITY UPLC-MS system
685 consisting of a Single Quadrupole Detector (SQD) Mass Spectrometer equipped with an
686 Electrospray Ionization interface and a Photodiode Array Detector from Waters Inc. (Milford, MA,
687 USA). Electrospray ionization in positive mode was used in the mass scan range 100-650Da. The
688 PDA range was 210-400nm. The analyses were run on an ACQUITY UPLC BEH C18 column
689 (100x2.1mmID, particle size 1.7µm) with a VanGuard BEH C18 pre-column (5x2.1mmID,
690 particle size 1.7µm), using 10mM NH_4OAc in H2O at pH 5 adjusted with CH_3COOH (A) and
691 10mM NH_4OAc in CH3CN-H2O (95:5) at pH 5 (B) as mobile phase.
692
693 ***In vitro* mouse plasma stability assay**
694 10mM DMSO stock solution of test compound was diluted 50-fold with DMSO-H2O (1:1) and
695 incubated at 37˚C for 2 h with mouse plasma added 5% DMSO (pre-heated at 37˚C for 10 min).
696 The final concentration was 2 µM. At each time point (0, 5, 15, 30, 60, 120 min), 50 µL of
697 incubation mixture was diluted with 200 µL cold CH3CN spiked with 200 nM of internal standard,
698 followed by centrifugation at 3.750 rpm for 20 min. The supernatant was further diluted with H2O
699 (1:1) for analysis. The concentration of test compound was quantified by LC/MS-MS on a Waters
700 ACQUITY UPLC/MS TQD system consisting of a Triple Quadrupole Detector (TQD) Mass

Spectrometer (MS) equipped with an Electrospray Ionization (ESI) interface. The analyses were run on an ACQUITY UPLC BEH C18 column (50 x 2.1 mmID, particle size 1.7 µm) with a VanGuard BEH C18 pre-column (5 x 2.1 mmID, particle size 1.7µm) at 40°C, using H2O + 0.1% HCOOH in H2O (A) and CH3CN + 0.1% HCOOH (B) as mobile phase. ESI was applied in positive mode. The response factors, calculated on the basis of the internal standard peak area, were plotted over time. Response factor versus time profiles were fitted with Prism (GraphPad Software, Inc., USA) to estimate compounds half-life (t½) in mouse plasma.

In vitro microsomal stability assay.

10mM DMSO stock solution of each compound was pre-incubated at 37°C for 15 min with mouse liver microsomes in 0.1M Tris-HCl buffer (pH 7.4). The final concentration was 4.6µM. After pre-incubation, the co-factors (NADPH, G6P, G6PDH and $MgCl_2$ pre-dissolved in 0.1M Tris-HCl) were added to the mixture and the incubation was continued at 37°C for 1h. At each time point (0, 5, 15, 30, 60min), 30µL of mixture was diluted with 200µL cold CH_3CN spiked with 200nM of internal standard, followed by centrifugation at 3500g for 15min. The supernatant was then further diluted with H_2O (1:1) for analysis. The concentration of each compound was quantified by LC/MS-MS on a Waters ACQUITY UPLC/MS TQD system consisting of a TQD (Triple Quadrupole Detector) Mass Spectrometer equipped with an Electrospray Ionization interface. The analyses were run on an ACQUITY UPLC BEH C18 (50x2.1mm ID, particle size 1.7µm) with a VanGuard BEH C18 pre-column (5x2.1mm ID, particle size 1.7µm) at 40°C, using 0.1% HCOOH in H_2O (A) and 0.1% HCOOH in CH_3CN (B) as mobile phases. The percentage of test compound remaining at each time point relative to the amount observed at t=0 was calculated. The half-lives

723 (t½) were determined by a one-phase decay equation using a non-linear regression of compound
724 concentration versus time.
725
726 **Mouse strains and PDX tumors**
727 All animal experiments were approved by the UC Irvine Institutional Animal Care and Use
728 Committee (IACUC) (AUP-17-230). NOD.Cg-*Prkdc*^{scid} *IL2rg*^{tm1Wjl}/SzJ (NSG) mice were
729 purchased from The Jackson Laboratories (stock number 005557). Human melanoma PDX tumors
730 (563396-261-R, 128128-338-R, 174941-126-T, 156681-154-R, 425362-254-T) were purchased
731 from Patient Derived Materials Repository (National Cancer Institute). Initial frozen tumors were
732 divided into evenly sized pieces and kept viable in ice cold RPMI (Corning) with 10% FBS. Small
733 incisions were made on both flanks of anesthetized NSG mice, with a single tumor piece placed
734 under the skin near each incision. Tumors were allowed to form and reach 10% body mass before
735 passaging into subsequent mice for drug studies. Excess portions of the tumor were frozen in RPMI
736 with 10% FBS and 10% DMSO. Following tumor placement, mice were monitored until the
737 tumors reached 100-200 mm^3 to start drug treatment.
738
739 **Drug treatment for PDX tumors**
740 ARN22089 was dissolved for 10 mg/kg doses in 100 µL of vehicle (80% Saline, 10% Tween80,
741 and 10% PEG400). Stocks of concentrated drug were frozen at -20°C for long term and kept at
742 4°C for up to 5 days. Mice were treated with 100 µL of vehicle or RhoJ inhibitor twice daily for
743 two weeks (morning and evening) through interperitoneal (IP) injections. Starting the same day as
744 injections, tumor volumes were measured by caliper twice a week. Estimated tumor volumes were
745 calculated by multiplying length by the width squared. At least four mice were imaged for each

PDX during the course of treatment and continued until the tumors reached endpoint (1500 mm^3). At endpoint, tumors were collected for histological analysis. For I.P. $BRAF^{V600E}$, $PTPN11^{N58S}$ tumors; $BRAF^{V600E}$ – Vemurafenib Resistant tumors; $BRAF^{V600E}$, $PTEN^{H259Y}$, $TP53^{C227Y}$ tumors both male and female mice used in vehicle and ARN22089 treatment groups. All of the $BRAF^{V600K}$ tumors were grown in female mice, while all of the $BRAF^{V600E}$, $PTEN^{H259Y}$, $TP53^{C227Y}$ tumors were grown in male mice. Statistical analysis was completed on the tumor growth measurements using a two-way ANOVA comparing treatment groups for each PDX over time with TukeyHSD pairwise comparisons between timepoints in R (version 3.5.3).

Intravenous (IV) tail vein injections of ARN22089 were prepared at 10 mg/kg, 25 mg/kg, and 50 mg/kg as described above. Female mice were treated by IV twice a week as the $BRAF^{V600E}$, $PTPN11^{N58S}$ tumors grew, for four weeks. Tumor and tissues were collected for histological analysis. Statistical analysis on tumor growth were completed in R (version 3.5.3) with a two-way ANOVA comparing treatment groups for each PDX over time with TukeyHSD pairwise comparisons between timepoints.

Tissue Collection

Once tumors reached endpoint, various tissues were collected including the tumors, liver, and lymph nodes. All organs were fixed overnight in 10% formalin prior to washing and an ethanol dehydration series. Fixed tissue was sent to the Experimental Tissue Resource (UCI Department of Pathology) for embedding and preliminary staining by H&E and S100. The percentage of tumor necrosis was determined from H&E sections by a pathologist blinded to treatment groups. Statistical test on necrosis scores was completed using a student's t-test in R (version 3.5.3).

769 **ACKNOWLEDGEMENTS**

770 We thank Jessica Shiu, Zachary Springs, Pezhman Mobasher, Terry Nguyen, Celine Saade,
771 Madeline McCanne, Katrina Huynh and and Giuliana Ottonello for their assistance with drug
772 treatments and DMPK evaluation. We thank the co-founders of Alyra Therapeutics, Mark
773 Benedyk and Alessandro Monge, for their advice and suggestions during the drug development
774 and validation studies. This work was supported by grants from the National Cancer Institute
775 (R01CA244571, U54CA217378) and the University of California, Irvine Chao Family
776 Comprehensive Cancer Center Anti-Cancer Challenge to AKG and The Italian Foundation for
777 Cancer Research (AIRC) (IG 18883 and IG 23679). JLF was supported by an NCI training grant
778 to the Cancer Research Institute at the University of California, Irvine (T32CA009054-37).
779 The RPPA Core is supported by NCI Grant # CA16672 and Dr. Yiling Lu's NIH R50 Grant #
780 R50CA221675: Functional Proteomics by Reverse Phase Protein Array in Cancer. This work was
781 made possible, in part, through access to the Genomics High Throughput Facility Shared Resource
782 of the Cancer Center Support Grant (P30CA-062203) at the University of California, Irvine and
783 NIH shared instrumentation grants 1S10RR025496-01, 1S10OD010794-01, and 1S10OD021718-
784 01. The content is solely the responsibility of the authors and does not necessarily represent the
785 official views of the National Institutes of Health.

786

787

788 **CONFLICT OF INTEREST**

789 Anand Ganesan and Marco De Vivo are co-founders of a company entitled Alyra Therapeutics
790 based on the technology presented in this manuscript.

791

REFERENCES

1 Maldonado, M. D. M. & Dharmawardhane, S. Targeting Rac and Cdc42 GTPases in Cancer. *Cancer Res* **78**, 3101-3111, doi:10.1158/0008-5472.CAN-18-0619 (2018).

2 Ruiz, R. *et al.* The RhoJ-BAD signaling network: An Achilles' heel for BRAF mutant melanomas. *PLoS Genet* **13**, e1006913, doi:10.1371/journal.pgen.1006913 (2017).

3 Wang, H. *et al.* Prominent Oncogenic Roles of EVI1 in Breast Carcinoma. *Cancer Res* **77**, 2148-2160, doi:10.1158/0008-5472.CAN-16-0593 (2017).

4 Kim, C. *et al.* Rho GTPase RhoJ is Associated with Gastric Cancer Progression and Metastasis. *J Cancer* **7**, 1550-1556, doi:10.7150/jca.15578 (2016).

5 Wilson, E. *et al.* RhoJ interacts with the GIT-PIX complex and regulates focal adhesion disassembly. *J Cell Sci* **127**, 3039-3051, doi:10.1242/jcs.140434 (2014).

6 Kim, C. *et al.* Vascular RhoJ is an effective and selective target for tumor angiogenesis and vascular disruption. *Cancer Cell* **25**, 102-117, doi:10.1016/j.ccr.2013.12.010 (2014).

7 Takase, H. *et al.* Genome-wide identification of endothelial cell-enriched genes in the mouse embryo. *Blood* **120**, 914-923, doi:10.1182/blood-2011-12-398156 (2012).

8 Boscher, C., Gaonac'h-Lovejoy, V., Delisle, C. & Gratton, J. P. Polarization and sprouting of endothelial cells by angiopoietin-1 require PAK2 and paxillin-dependent Cdc42 activation. *Mol Biol Cell* **30**, 2227-2239, doi:10.1091/mbc.E18-08-0486 (2019).

9 El Atat, O., Fakih, A. & El-Sibai, M. RHOG Activates RAC1 through CDC42 Leading to Tube Formation in Vascular Endothelial Cells. *Cells* **8**, doi:10.3390/cells8020171 (2019).

10 Xiao, X. H. *et al.* Regulating Cdc42 and Its Signaling Pathways in Cancer: Small Molecules and MicroRNA as New Treatment Candidates. *Molecules* **23**, doi:10.3390/molecules23040787 (2018).

11 Lu, H. *et al.* PAK signalling drives acquired drug resistance to MAPK inhibitors in BRAF-mutant melanomas. *Nature* **550**, 133-136, doi:10.1038/nature24040 (2017).

12 Han, S. W. *et al.* RNA editing in RHOQ promotes invasion potential in colorectal cancer. *J Exp Med* **211**, 613-621, doi:10.1084/jem.20132209 (2014).

13 Bridges, E. *et al.* RHOQ is induced by DLL4 and regulates angiogenesis by determining the intracellular route of the Notch intracellular domain. *Angiogenesis* **23**, 493-513, doi:10.1007/s10456-020-09726-w (2020).

14 Haga, R. B. & Ridley, A. J. Rho GTPases: Regulation and roles in cancer cell biology. *Small GTPases* **7**, 207-221, doi:10.1080/21541248.2016.1232583 (2016).

15 Zins, K., Gunawardhana, S., Lucas, T., Abraham, D. & Aharinejad, S. Targeting Cdc42 with the small molecule drug AZA197 suppresses primary colon cancer growth and prolongs survival in a preclinical mouse xenograft model by downregulation of PAK1 activity. *J Transl Med* **11**, 295, doi:10.1186/1479-5876-11-295 (2013).

16 Pelish, H. E. *et al.* Secramine inhibits Cdc42-dependent functions in cells and Cdc42 activation in vitro. *Nat Chem Biol* **2**, 39-46, doi:10.1038/nchembio751 (2006).

17 Hampsch, R. A. *et al.* Therapeutic sensitivity to Rac GTPase inhibition requires consequential suppression of mTORC1, AKT, and MEK signaling in breast cancer. *Oncotarget* **8**, 21806-21817, doi:10.18632/oncotarget.15586 (2017).

18 Pleines, I. *et al.* Defective tubulin organization and proplatelet formation in murine megakaryocytes lacking Rac1 and Cdc42. *Blood* **122**, 3178-3187, doi:10.1182/blood-2013-03-487942 (2013).

19 Dutting, S. *et al.* Critical off-target effects of the widely used Rac1 inhibitors NSC23766 and EHT1864 in mouse platelets. *J Thromb Haemost* **13**, 827-838, doi:10.1111/jth.12861 (2015).

20 Sawada, N., Li, Y. & Liao, J. K. Novel aspects of the roles of Rac1 GTPase in the cardiovascular system. *Curr Opin Pharmacol* **10**, 116-121, doi:10.1016/j.coph.2009.11.004 (2010).

21 O'Bryan, J. P. Pharmacological targeting of RAS: Recent success with direct inhibitors. *Pharmacol Res* **139**, 503-511, doi:10.1016/j.phrs.2018.10.021 (2019).

22 De Vivo, M. & Cavalli, A. Recent advances in dynamic docking for drug discovery. *WIREs Computational Molecular Science* **7**, e1320, doi:https://doi.org/10.1002/wcms.1320 (2017).

23 De Vivo, M., Masetti, M., Bottegoni, G. & Cavalli, A. Role of Molecular Dynamics and Related Methods in Drug Discovery. *J Med Chem* **59**, 4035-4061, doi:10.1021/acs.jmedchem.5b01684 (2016).

24 Hoffman, G. R., Nassar, N. & Cerione, R. A. Structure of the Rho family GTP-binding protein Cdc42 in complex with the multifunctional regulator RhoGDI. *Cell* **100**, 345-356, doi:10.1016/s0092-8674(00)80670-4 (2000).

25 Ha, B. H. & Boggon, T. J. CDC42 binds PAK4 via an extended GTPase-effector interface. *Proc Natl Acad Sci U S A* **115**, 531-536, doi:10.1073/pnas.1717437115 (2018).

26 Morreale, A. *et al.* Structure of Cdc42 bound to the GTPase binding domain of PAK. *Nat Struct Biol* **7**, 384-388, doi:10.1038/75158 (2000).

27 LeCour, L., Jr. *et al.* The Structural Basis for Cdc42-Induced Dimerization of IQGAPs. *Structure* **24**, 1499-1508, doi:10.1016/j.str.2016.06.016 (2016).

28 La Sala, G., Decherchi, S., De Vivo, M. & Rocchia, W. Allosteric Communication Networks in Proteins Revealed through Pocket Crosstalk Analysis. *ACS Central Science* **3**, 949-960, doi:10.1021/acscentsci.7b00211 (2017).

29 Ho, H. *et al.* RhoJ regulates melanoma chemoresistance by suppressing pathways that sense DNA damage. *Cancer Res* **72**, 5516-5528, doi:10.1158/0008-5472.CAN-12-0775 (2012).

30 Friesland, A. *et al.* Small molecule targeting Cdc42-intersectin interaction disrupts Golgi organization and suppresses cell motility. *Proc Natl Acad Sci U S A* **110**, 1261-1266, doi:10.1073/pnas.1116051110 (2013).

31 Umbayev, B. *et al.* Elevated levels of the small GTPase Cdc42 induces senescence in male rat mesenchymal stem cells. *Biogerontology* **19**, 287-301, doi:10.1007/s10522-018-9757-5 (2018).

32 Kim, J. M., Kim, M. Y., Lee, K. & Jeong, D. Distinctive and selective route of PI3K/PKCalpha-PKCdelta/RhoA-Rac1 signaling in osteoclastic cell migration. *Mol Cell Endocrinol* **437**, 261-267, doi:10.1016/j.mce.2016.08.042 (2016).

33 Rudolph, M. G. *et al.* Thermodynamics of Ras/effector and Cdc42/effector interactions probed by isothermal titration calorimetry. *J Biol Chem* **276**, 23914-23921, doi:10.1074/jbc.M011600200 (2001).

34 Lepur, A. & Vugrek, O. Bimolecular Fluorescence Complementation to Visualize Protein-Protein Interactions in Human Cells Based on Gateway Cloning Technology. *Methods Mol Biol* **1794**, 259-267, doi:10.1007/978-1-4939-7871-7_17 (2018).

35 Chou, M. M. & Blenis, J. The 70 kDa S6 kinase complexes with and is activated by the Rho family G proteins Cdc42 and Rac1. *Cell* **85**, 573-583, doi:10.1016/s0092-8674(00)81257-x (1996).

36 Ferrari, S., Bandi, H. R., Hofsteenge, J., Bussian, B. M. & Thomas, G. Mitogen-activated 70K S6 kinase. Identification of in vitro 40 S ribosomal S6 phosphorylation sites. *J Biol Chem* **266**, 22770-22775 (1991).

37 Basak, C. *et al.* NF-kappaB- and C/EBPbeta-driven interleukin-1beta gene expression and PAK1-mediated caspase-1 activation play essential roles in interleukin-1beta release from Helicobacter pylori lipopolysaccharide-stimulated macrophages. *J Biol Chem* **280**, 4279-4288, doi:10.1074/jbc.M412820200 (2005).

38 Hsu, Y. H., Moya, M. L., Hughes, C. C., George, S. C. & Lee, A. P. A microfluidic platform for generating large-scale nearly identical human microphysiological vascularized tissue arrays. *Lab Chip* **13**, 2990-2998, doi:10.1039/c3lc50424g (2013).

39 Moya, M. L., Hsu, Y. H., Lee, A. P., Hughes, C. C. & George, S. C. In vitro perfused human capillary networks. *Tissue Eng Part C Methods* **19**, 730-737, doi:10.1089/ten.TEC.2012.0430 (2013).

40 Wang, X. *et al.* Engineering anastomosis between living capillary networks and endothelial cell-lined microfluidic channels. *Lab Chip* **16**, 282-290, doi:10.1039/c5lc01050k (2016).

41 Sobrino, A. *et al.* 3D microtumors in vitro supported by perfused vascualr networks. *Sci. Reports.* **6**, 31589, doi:DOI: 10.1038/srep31589 (2016).

42 Kalyaanamoorthy, S. & Barakat, K. H. Development of Safe Drugs: The hERG Challenge. *Med Res Rev* **38**, 525-555, doi:10.1002/med.21445 (2018).

43 Olson, M. F. Rho GTPases, their post-translational modifications, disease-associated mutations and pharmacological inhibitors. *Small GTPases* **9**, 203-215, doi:10.1080/21541248.2016.1218407 (2018).

44 Croise, P., Estay-Ahumada, C., Gasman, S. & Ory, S. Rho GTPases, phosphoinositides, and actin: a tripartite framework for efficient vesicular trafficking. *Small GTPases* **5**, e29469, doi:10.4161/sgtp.29469 (2014).

45 Lu, H. *et al.* Recent advances in the development of protein-protein interactions modulators: mechanisms and clinical trials. *Signal Transduct Target Ther* **5**, 213, doi:10.1038/s41392-020-00315-3 (2020).

46 Bery, N. *et al.* BRET-based RAS biosensors that show a novel small molecule is an inhibitor of RAS-effector protein-protein interactions. *Elife* **7**, doi:10.7554/eLife.37122 (2018).

47 Quevedo, C. E. *et al.* Small molecule inhibitors of RAS-effector protein interactions derived using an intracellular antibody fragment. *Nat Commun* **9**, 3169, doi:10.1038/s41467-018-05707-2 (2018).

48 Maldonado, M. D. M., Medina, J. I., Velazquez, L. & Dharmawardhane, S. Targeting Rac and Cdc42 GEFs in Metastatic Cancer. *Front Cell Dev Biol* **8**, 201, doi:10.3389/fcell.2020.00201 (2020).

49 Wang, Z. *et al.* p21-activated kinase 1 (PAK1) can promote ERK activation in a kinase-independent manner. *J Biol Chem* **288**, 20093-20099, doi:10.1074/jbc.M112.426023 (2013).

50 Coles, L. C. & Shaw, P. E. PAK1 primes MEK1 for phosphorylation by Raf-1 kinase during cross-cascade activation of the ERK pathway. *Oncogene* **21**, 2236-2244, doi:10.1038/sj.onc.1205302 (2002).

51 Gan, J. *et al.* Growth hormone-releasing hormone receptor antagonists inhibit human gastric cancer through downregulation of PAK1-STAT3/NF-kappaB signaling. *Proc Natl Acad Sci U S A* **113**, 14745-14750, doi:10.1073/pnas.1618582114 (2016).

52 Yoshida, S. *et al.* Tumor Angiogenic Inhibition Triggered Necrosis (TAITN) in Oral Cancer. *Cells* **8**, doi:10.3390/cells8070761 (2019).

53 Lipinski, C. A. Lead- and drug-like compounds: the rule-of-five revolution. *Drug Discov Today Technol* **1**, 337-341, doi:10.1016/j.ddtec.2004.11.007 (2004).

54 Jorgensen, W. L., Chandrasekhar, J., Madura, J. D., Impey, R. W. & Klein, M. L. Comparison of simple potential functions for simulating liquid water. *The Journal of Chemical Physics* **79**, 926-935, doi:10.1063/1.445869 (1983).

55 Maier, J. A. *et al.* ff14SB: Improving the Accuracy of Protein Side Chain and Backbone Parameters from ff99SB. *J Chem Theory Comput* **11**, 3696-3713, doi:10.1021/acs.jctc.5b00255 (2015).

56 Singh, U. C. & Kollman, P. A. An approach to computing electrostatic charges for molecules. *Journal of Computational Chemistry* **5**, 129-145, doi:https://doi.org/10.1002/jcc.540050204 (1984).

57 Meagher, K. L., Redman, L. T. & Carlson, H. A. Development of polyphosphate parameters for use with the AMBER force field. *J Comput Chem* **24**, 1016-1025, doi:10.1002/jcc.10262 (2003).

58 Allner, O., Nilsson, L. & Villa, A. Magnesium Ion-Water Coordination and Exchange in Biomolecular Simulations. *J Chem Theory Comput* **8**, 1493-1502, doi:10.1021/ct3000734 (2012).

59 Joung, I. S. & Cheatham, T. E. Determination of Alkali and Halide Monovalent Ion Parameters for Use in Explicitly Solvated Biomolecular Simulations. *The Journal of Physical Chemistry B* **112**, 9020-9041, doi:10.1021/jp8001614 (2008).

60 Case D. A., B. K., Ben-Shalom I. Y., Brozell S. R., Cerutti D. S., Cheatham T.E. III, Cruzeiro V. W. D., Darden T. A., Duke R. E., Giambasu G., Gilson M. K., Gohlke H., Goetz A. W. ,Harris R., Izadi S., Izmailov S. A., Kasavajhala K., Kovalenko A., Krasny R., Kurtzman T., Lee T. S., LeGrand S., Li P., Lin C., Liu J., Luchko T., Luo R., Man V., Merz K M., Miao Y., Mikhailovskii O., Monard G., Nguyen H., Onufriev A., Pan F., Pantano S., Qi R., Roe D. R., Roitberg A., Sagui C., Schott-Verdugo S., Shen J., Simmerling C., Skrynnikov N. R., Smith J., Swails J., Walker R. C., Wang J., Wilson L., Wolf R. M., Wu X., Xiong Y., Xue Y, York D. M., Kollman P.A. AMBER 2020, University of California, San Francisco. (2020).

61 Andrea, T. A., Swope, W. C. & Andersen, H. C. The role of long ranged forces in determining the structure and properties of liquid water. *The Journal of Chemical Physics* **79**, 4576-4584, doi:10.1063/1.446373 (1983).

62 Geoghegan, K. F. *et al.* Spontaneous alpha-N-6-phosphogluconoylation of a "His tag" in Escherichia coli: the cause of extra mass of 258 or 178 Da in fusion proteins. *Anal Biochem* **267**, 169-184, doi:10.1006/abio.1998.2990 (1999).

63 Trapnell, C., Pachter, L. & Salzberg, S. L. TopHat: discovering splice junctions with RNA-Seq. *Bioinformatics* **25**, 1105-1111, doi:10.1093/bioinformatics/btp120 (2009).

64 Trapnell, C. *et al.* Transcript assembly and quantification by RNA-Seq reveals unannotated transcripts and isoform switching during cell differentiation. *Nat Biotechnol* **28**, 511-515, doi:10.1038/nbt.1621 (2010).

65 Kim, D., Paggi, J. M., Park, C., Bennett, C. & Salzberg, S. L. Graph-based genome alignment and genotyping with HISAT2 and HISAT-genotype. *Nat Biotechnol* **37**, 907-915, doi:10.1038/s41587-019-0201-4 (2019).

66 Kluin, R. J. C. *et al.* XenofilteR: computational deconvolution of mouse and human reads in tumor xenograft sequence data. *BMC Bioinformatics* **19**, 366, doi:10.1186/s12859-018-2353-5 (2018).

67 Love, M. I., Huber, W. & Anders, S. Moderated estimation of fold change and dispersion for RNA-seq data with DESeq2. *Genome Biol* **15**, 550, doi:10.1186/s13059-014-0550-8 (2014).

68 Szklarczyk, D. *et al.* STRING v11: protein-protein association networks with increased coverage, supporting functional discovery in genome-wide experimental datasets. *Nucleic Acids Res* **47**, D607-D613, doi:10.1093/nar/gky1131 (2019).

69 Dennis, G., Jr. *et al.* DAVID: Database for Annotation, Visualization, and Integrated Discovery. *Genome Biol* **4**, P3 (2003).

70 Bagci, H. *et al.* Mapping the proximity interaction network of the Rho-family GTPases reveals signalling pathways and regulatory mechanisms. *Nat Cell Biol* **22**, 120-134, doi:10.1038/s41556-019-0438-7 (2020).

71 Ziman, M., O'Brien, J. M., Ouellette, L. A., Church, W. R. & Johnson, D. I. Mutational analysis of CDC42Sc, a Saccharomyces cerevisiae gene that encodes a putative GTP-binding protein involved in the control of cell polarity. *Mol Cell Biol* **11**, 3537-3544, doi:10.1128/mcb.11.7.3537-3544.1991 (1991).

72 Vignal, E. *et al.* Characterization of TCL, a new GTPase of the rho family related to TC10 andCcdc42. *J Biol Chem* **275**, 36457-36464, doi:10.1074/jbc.M003487200 (2000).

Figure 1

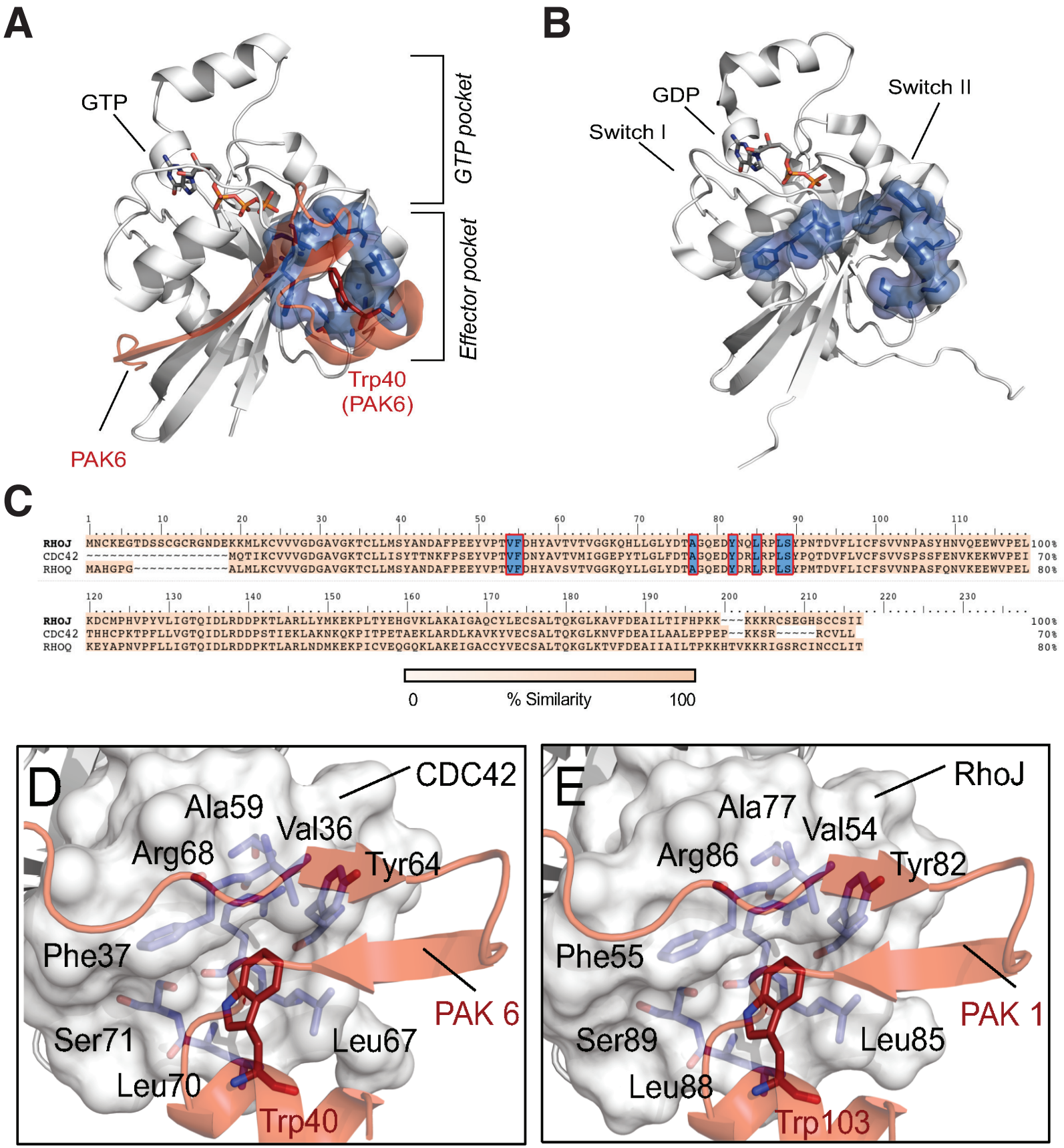

Figure 1: Characterization of a RHOJ/CDC42 allosteric drug binding pocket located at the effector interaction interface. A) GTP-bound state of the effector pocket (blue) interacting with Trp40 (red) of PAK6 - PDBid 2ODB. **B)** Unfolded conformation of the effector pocket in the GDP-bound state - PDBid: 1DOA. **C)** Amino acid sequences alignment of RHOJ, CDC42 and RHOQ. The residues defining the drug binding pocket are highlighted in blue. **D)** Close-up view of the CDC42-PAK6 interaction interface. Interactions between Trp40 (red) of PAK6 (transparent red) and the effector binding pocket (light blue) of CDC42 (grey) are shown. **E)** Close-up view of the RHOJ-PAK1 interaction interface. For comparison, modeling of the interaction between Trp103 (red) of PAK1 (transparent red) and the effector binding pocket (light blue) of RHOJ (grey) is shown.

Figure 2

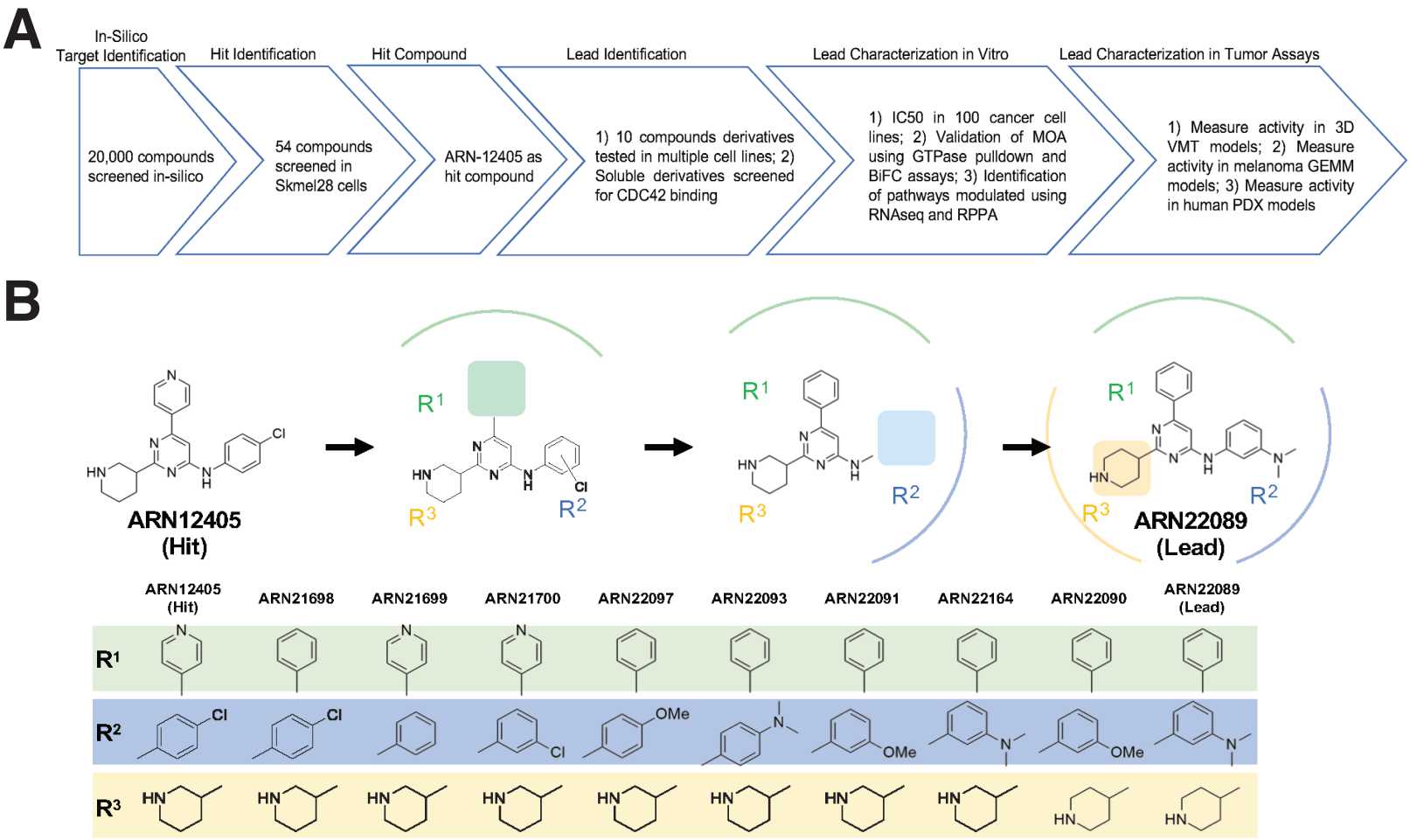

C

	SKM28 (μM)	R Squared	WM3248 (μM)	R Squared	Skmel3 (μM)	R Squared	A375 (μM)	R Squared	SW480 (μM)	R Squared	S kinetic (μM)	t1/2 Plasma (min)	t1/2 Microsomes (min)
ARN-12405	16.37	0.9936	14.38	0.9633	13.47	0.9947	15.27	0.9786	14.8	0.9698	222±6	>120	48
ARN-21698	10.21	0.9112	8.423	0.939	6.3	0.9844	10.94	0.9872	11.91	0.9866	<1	>120	46
ARN-21699	ND	ND	23.08	0.4995	26.87	0.9331	22.47	0.4555	26.78	0.5829	NA	NA	NA
ARN-21700	38.31	0.9711	30.85	0.9688	10.24	0.9768	11.33	0.9754	25.28	0.9612	NA	NA	NA
ARN-22097	>50	0.9793	27.53	0.9881	13.27	0.9264	22.94	0.9398	25.04	0.9858	NA	NA	NA
ARN-22093	45.02	0.9937	12.76	0.9478	11.84	0.9019	13.14	0.9761	17.66	0.9752	246±2	>120	43
ARN-22091	24.2	0.9664	11.28	0.9932	11.77	0.9685	12.52	0.963	17.75	0.9933	237±1	>120	21
ARN-22164	31.4	0.9794	10.97	0.9441	8.138	0.9174	14.61	0.9741	11.4	0.9961	>250	119±12	20
ARN-22090	38.12	0.9432	9.468	0.9478	4.588	0.9776	9.787	0.9941	10.49	0.9824	>250	>120	27
ARN-22089	24.8	0.9936	4.523	0.9951	4.257	0.9512	4.92	0.9521	8.608	0.986	250±4	71	27

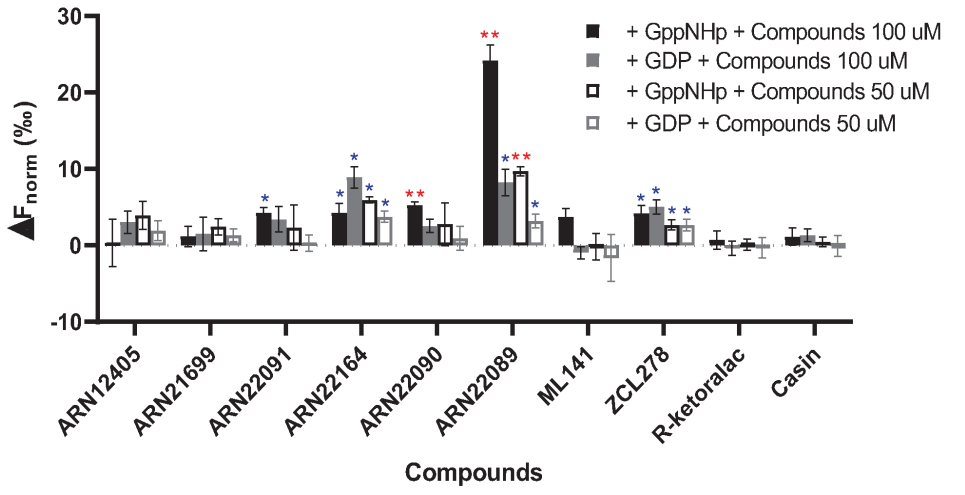

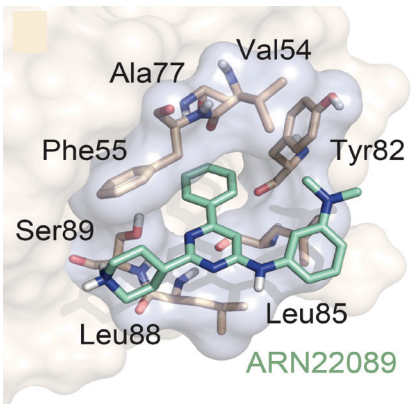

Figure 2: Structure-based screening identifies RHOJ/CDC42 allosteric inhibitors. A) Flow diagram of the screening steps to identify RHOJ/CDC42 allosteric inhibitors. **B)** Chemical structures of the hit and synthesized derivatives. Names of the compounds and structures of the indicated R side chains are denoted below. **C)** Table of IC50s, solubilities, and plasma and mouse microsomal half-life of lead and synthesized derivatives. Detailed IC50 curves are shown in **Figure S2A**. **D)** MST was used to screen for binding of the hit, derivatives, and known CDC42 inhibitors to a His-tagged CDC42 fragment. The graph displays the difference in normalized fluorescence (ΔF_{norm} [%] = $\Delta F_{hot}/F_{cold}$) at 1.5-2.5 sec between protein:compound sample and a protein only sample at the indicated drug concentrations after loading with the indicated nucleotides. A single asterisk highlights binding with signal to noise ratio equal or higher than 5. Double asterisks are used for binding with signal to noise ratio higher than 12. **E)** Model structure of lead compound bound to the allosteric drug binding pocket of CDC42/RHOJ.

Figure 3

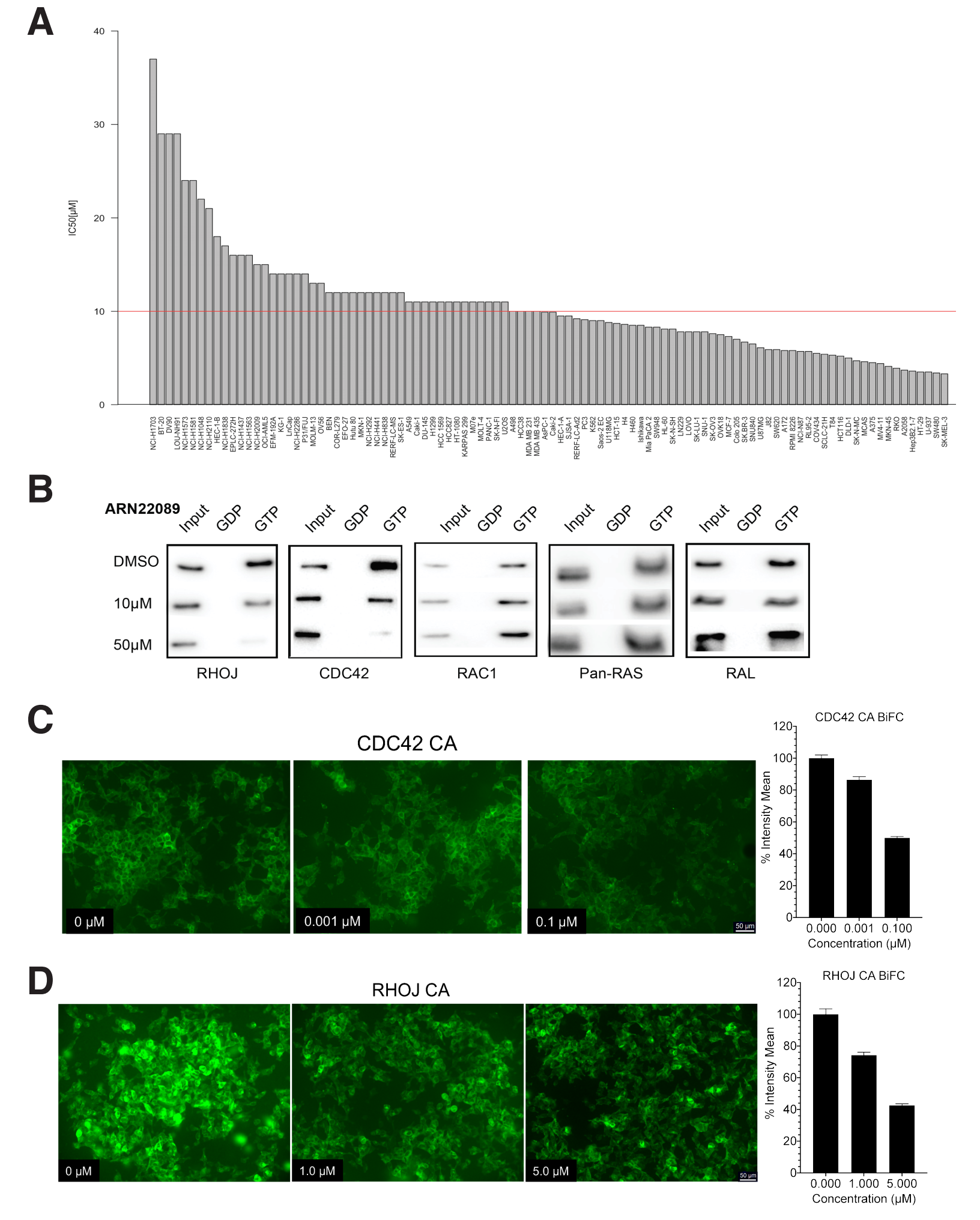

Figure 3: ARN22089 has broad spectrum anti-cancer activity and selectively blocks RHOJ/CDC42 effector interactions. A) Bar graph shows IC50 values of ARN22089 in 100 cancer cell lines. **B)** ARN22089 selectively blocks CDC42 effector interactions. WM3248 cells were treated with ARN22089 for 24 hours and lysates were subjected to pulldown assays with PAK1 and RAF1 to measure the ability of the compound to block RHOJ, CDC42, RAC1, RAS, or RAL effector interactions. **(C**) CDC42 and (**D**) RHOJ BiFC cells were treated with 2 μg/mL of DOX to induce CDC42/RHOJ and PAK1 expression and treated with the indicated doses of ARN22089 for 24 and 8 h, respectively. Bar graphs, far right for (**C**) and (**D**), show mean percent GFP intensity for each condition. The 0 μM condition was set to 100%. No DOX condition was used for background subtraction.

Figure 4

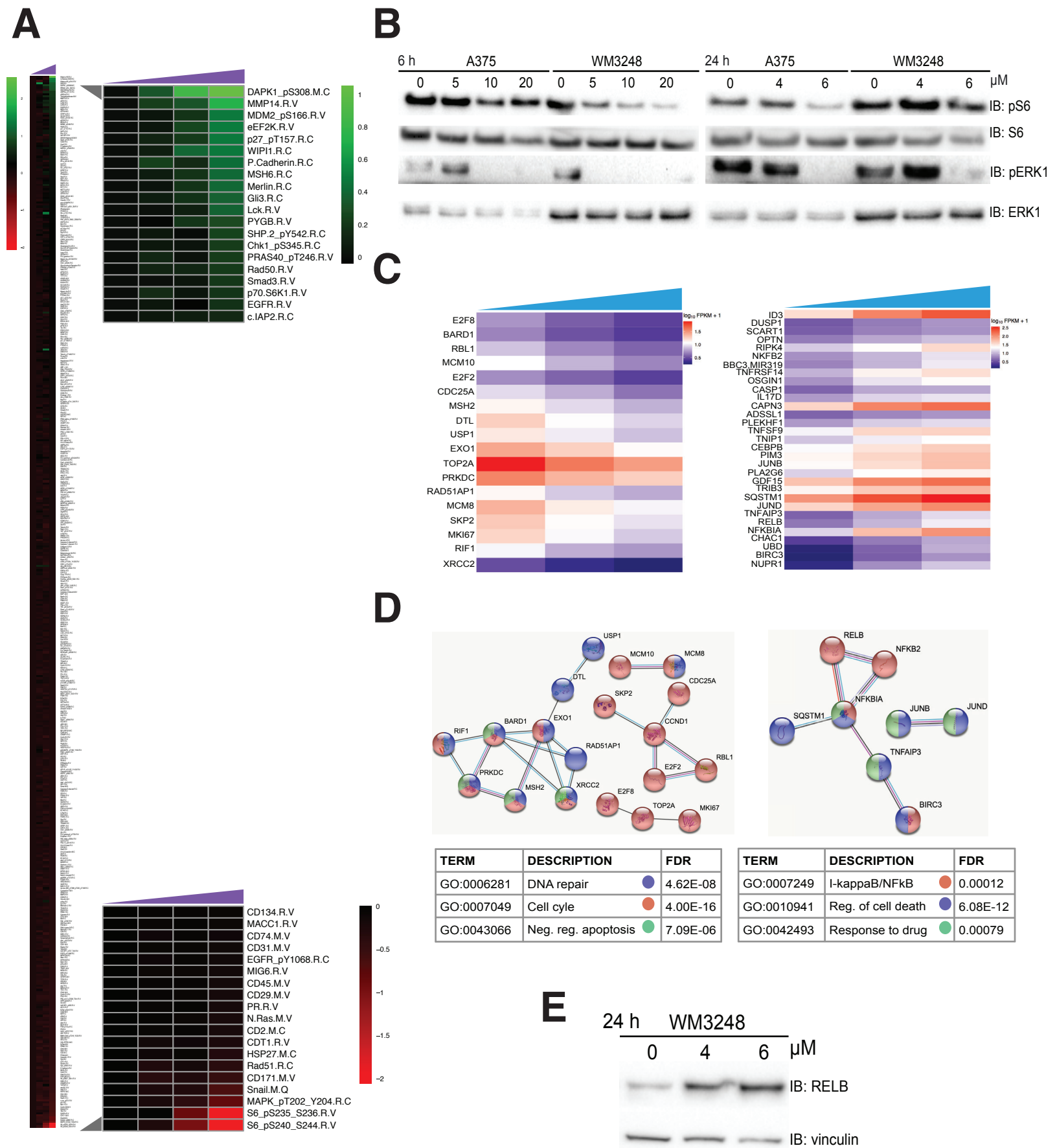

TERM	DESCRIPTION	FDR
GO:0006281	DNA repair	4.62E-08
GO:0007049	Cell cyle	4.00E-16
GO:0043066	Neg. reg. apoptosis	7.09E-06

TERM	DESCRIPTION	FDR
GO:0007249	I-kappaB/NFkB	0.00012
GO:0010941	Reg. of cell death	6.08E-12
GO:0042493	Response to drug	0.00079

Figure 4: Characterization of the activity of ARN22089 in melanoma cells. A) RPPA heatmap showing effects of drug treatment on protein accumulation/phosphorylation. Colors represents values of each treated dose normalized to vehicle (0 μM) (see **Table S6**). Left, heatmap shows results for 486 proteins assayed. Right, insets include proteins that were significantly modulated by drug treatment (see **Table S7**). **B)** WM3248 or A375 cells were treated with the indicated doses of ARN22089 and the accumulation of pS6 and pERK (targets significantly modulated in the RPPA analysis) were measured by immunoblotting. **C)** Profile heatmaps of mRNA sequences that were differentially transcribed after drug treatment (cutoff q-value < 0.05, **Table S8**). **D)** Protein-protein interactions networks modulated by drug treatment. Significant genes shown in (**C**) were subjected to STRING analysis to identify protein-protein interaction networks. Nodes are color coded based on Gene ontology analysis shown in the table below. **E)** Immunoblot for RELB from WM3248 cells that were treated with the indicated doses of ARN22089 for 24 h.

Figure 5

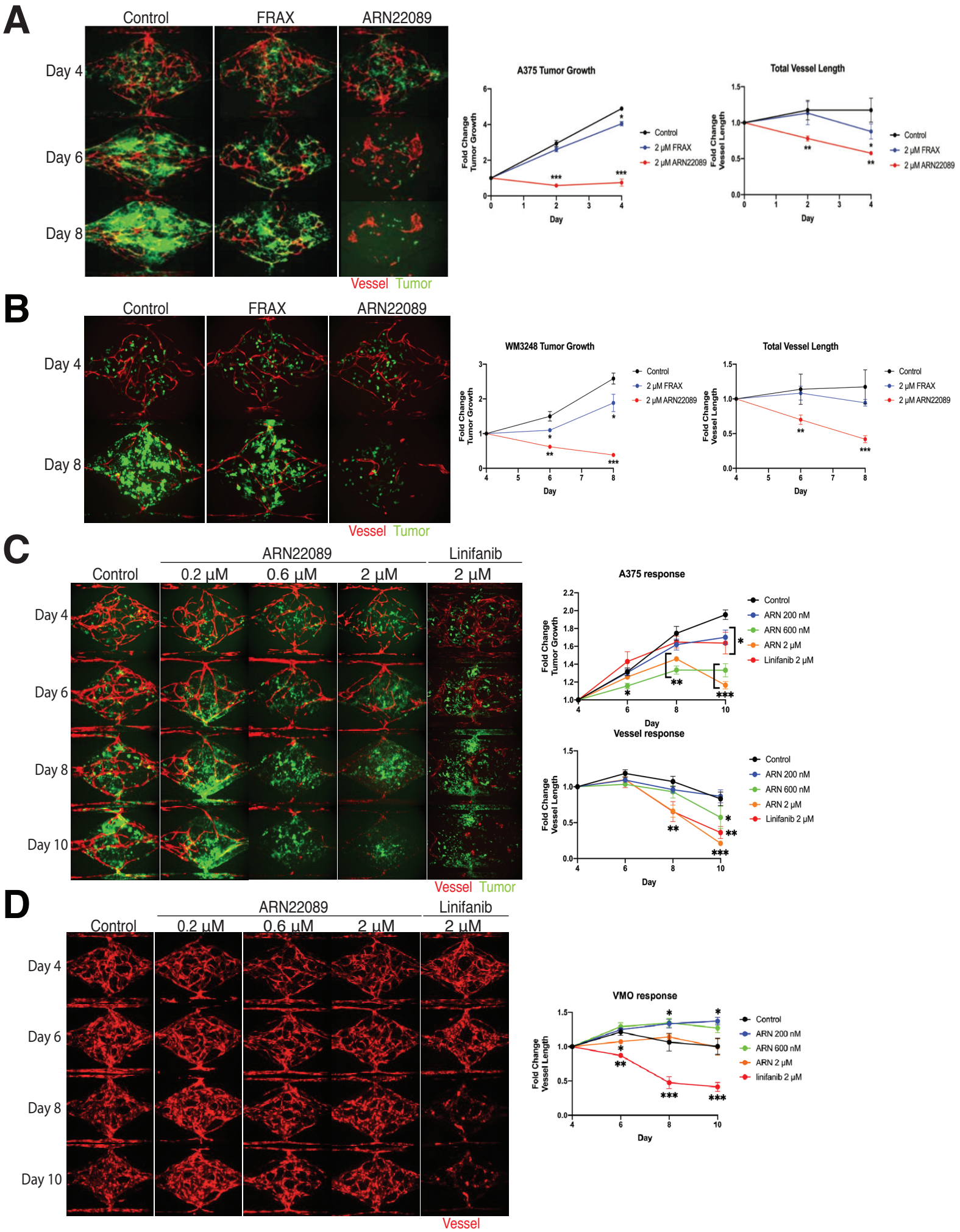

Figure 5: ARN22089 inhibits tumor growth in a Vascularized Microtumor (VMT) model. Representative micrographs of **(A)** A375 or **(B)** WM3248 VMTs (organoids that contain cancer cells and endothelial cells) treated with control, 2 μM FRAX or ARN22089. Quantification of tumor cell growth and vessel length shown on right. **C)** Micrographs VMT of WM3248 treated with increasing concentration of ARN22089, corresponding quantification shown on right. The angiogenesis inhibitor Linifanib at 2 μM is shown as a comparison. **D)** Micrographs of VMOs (organoids with only endothelial cells) treated with increasing concentrations of ARN22089 or Linifanib and corresponding quantification of vessel length is shown.

Figure 6

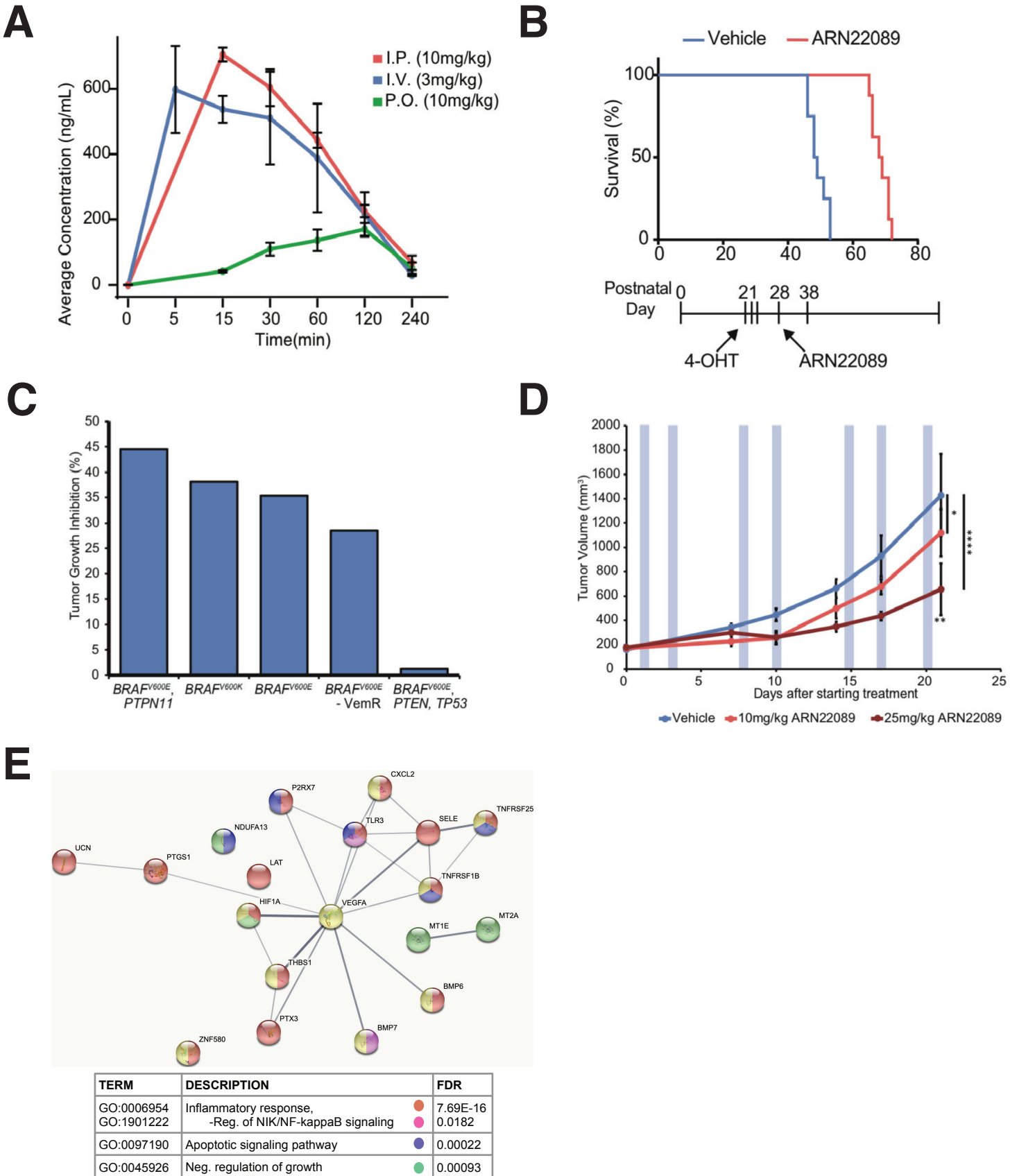

TERM	DESCRIPTION	FDR
GO:0006954 GO:1901222	Inflammatory response, -Reg. of NIK/NF-kappaB signaling	7.69E-16 0.0182
GO:0097190	Apoptotic signaling pathway	0.00022
GO:0045926	Neg. regulation of growth	0.00093
GO:0042127	Regulation of cell population proliferation	0.00021

Figure 6. ARN22089 inhibits tumor growth in mouse models. **A)** ARN22089 delivered at 10mg/kg I.P. and 3mg/kg I.V. has drug like properties. PK of compounds was calculated as described in the methods. Complete data is shown in Fig S5F. **B)** ARN22089 inhibits melanoma development in a murine *BRAF*^{V600E}, *PTEN*$^{flox/flox}$, *Tyr:Cre*^{ERT2} model. Melanoma was induced at P21-23 with topical treatment of 25mg/mL 4-OHT. Mice were then treated with vehicle (blue) or 10mg/kg I.P. ARN22089 (red) for 10 days between P28 -P38. **C)** ARN22089 inhibits tumor growth in *BRAF* mutant PDX tumor models (listed by verified mutations). Mice were treated for 14 days with 10mg/kg I.P. ARN22089 starting when PDX tumors reached 150-200mm^3. Tumor growth inhibition was compared with matched vehicle treated mice (see also Figure S6A,B). **D)** ARN22089 inhibits tumor growth in a dose responsive manner. *BRAF*^{V600E}, *PTPN11* PDX tumors were treated with vehicle (blue), 10mg/kg ARN22089 (light red), or 25mg/kg ARN22089 (dark red) twice weekly after tumors reached 150-200mm^3, blue shaded boxes denote I.V. treatments (see also **Figure S5**). **E)** RNA from the tumors described in (**D**) were sequenced. STRING was used to identify differentially expressed protein-protein interaction networks. Nodes are color coded based on Gene Ontology indicated in the table below.